



## Supplementary Materials for

### **Ultrafast neuronal imaging of dopamine dynamics with designed genetically encoded sensors**

Tommaso Patriarchi, Jounhong Ryan Cho, Katharina Merten, Mark W. Howe,  
Aaron Marley, Wei-Hong Xiong, Robert W. Folk, Gerard Joey Broussard,  
Ruqiang Liang, Min Jee Jang, Haining Zhong, Daniel Dombeck, Mark von Zastrow,  
Axel Nimmerjahn, Viviana Gradinaru, John T. Williams, Lin Tian\*

\*Corresponding author. Email: lintian@ucdavis.edu

Published 31 May 2018 on *Science* First Release  
DOI: 10.1126/science.aat4422

#### **This PDF file includes:**

Materials and Methods

Figs. S1 to S16

Captions for data S1 to S3

References

#### **Other supplementary material for this manuscript includes:**

Data S1 to S3

## **Materials and Methods**

### Molecular Cloning

All constructs were designed using circular polymerase extension cloning (CPEC) (37), restriction cloning, and gBlock gene fragments (Integrated DNA Technologies). Sequences coding for a hemagglutinin (HA) cleavable secretion motif and a FLAG epitope were placed at the 5'-end of the construct as in (23). HindIII and NotI cut sites were placed at the 5'- and 3'-end, respectively, for cloning into pEGFP-N1 (Addgene) to generate all pCMV constructs. BamHI and HindIII sites were introduced via PCR for final subcloning onto pAAV.*hSynapsin1* and pAAV.*CAG* vectors.

To maximize coupling between conformational changes and chromophore fluorescence, we chose to use a cpGFP module (LSS-LE-cpGFP-LP-DQL) from GCaMP6 (18) for insertion into DRD1 via CPEC. For screening linker variants, we generated a linker library by first creating an insert DNA carrying a 2 aminoacid-long randomized linker on each side of cpGFP (LSS-xx-cpGFP-xx-DQL). Single colonies were manually picked and grown overnight as described in (38). All sensor sequences generated in this study are listed in the Supplementary Data S1 file.

### Structural modeling and sequence alignments

Sequence alignments were performed using Jalview software (UK) (39) using a percentage identity color map. Inactive conformation of the sensor was predicted with rosetta\_cm protocol of rosetta 3 (version 2015.31) (40). Primary sequence of sensor design was threaded with partial thread routine onto template PDB structures of inactive  $\beta_2$  adrenergic receptor (41) (ID: 2RH1) and unbound state of GCaMP3 (42) (ID: 4IK3). The threaded structures were then hybridized together with rosetta\_cm protocol for membrane protein (43). A total of 374 PDB structures

were generated by rosetta\_script routine. Structure with lowest total score was considered the final model.

### Cell culture, imaging and quantification

HEK293T cells (ATCC #1573) and U2OS cells (ATCC #HTB-96) used in this study were cultured and transfected as in (23, 44). Primary hippocampal neurons were freshly isolated as previously described (45). Neurons were infected using AAVs ( $1 \times 10^9$  GC/ml) at DIV5, two weeks prior to imaging. Prior to imaging, cells were washed with HBSS (Life Technologies). Cell imaging was performed using a 40X oil-based objective on an inverted Zeiss Observer LSN710 confocal microscope with 488/513 ex/em wavelengths. For testing sensor responses, neurotransmitters/drugs were directly applied to the bath during the imaging session. For neurotransmitter titrations, a dual buffer gravity-driven perfusion system was used to exchange buffers between different drug concentrations. Surface labeling was achieved as described previously (23, 44). One-photon emission spectrum for the sensors was determined using the lambda-scan function of the confocal microscope. Two-photon emission spectrum was obtained with a 40X water-based objective on a SliceScope (Scientifica) and was used to obtain the normalized two-photon cross-section using a custom-made script on MATLAB. For ROIs selection, masks were generated either on the cell membrane or around the cytosol, depending on the experiment, using the threshold function in Fiji. We calculated spatial movies and images of

$\Delta F/F$  in response to an applied ligand as  $F(t) - \bar{F}_{baseline} / \bar{F}_{baseline}$  with  $F(t)$  the pixel-wise

fluorescence value at each time,  $t$ , and mean fluorescence in time points prior to ligand application,  $\bar{F}_{baseline}$ . To avoid the possibility of infinite pixel values, we added a small offset to each pixel in  $\bar{F}_{baseline}$ . Based on the  $\Delta F/F$  maps, we calculated a corresponding SNR map as

$\Delta F/F \times \sqrt{\bar{F}_{baseline}}$ .  $\Delta FF$  heatmaps were generated using a custom MATLAB script. Surface expression of sensors was quantified as the ratio of membrane fluorescence over cytoplasm fluorescence. For titration curves, Kd values were obtained by fitting the data with a Hill function on Igor Pro (WaveMetrics).

### Dopamine-uncaging

Uncaging experiments on neuronal dendrites were performed in the presence of 100  $\mu\text{M}$  caged-dopamine (carboxynitroveratryl-DA, CNV-DA (46)) in the HBSS. Optical recordings were performed at 153 ms/frame scan rate. Uncaging was achieved by shining 405 nm light (40% laser power) on a 2  $\mu\text{m}$  wide circular region selected 10  $\mu\text{m}$  away from the dendrite surface.

### Internalization assay with flow cytometry

24 hours post transfection, cells were re-plated onto 6 well dishes. The following day, surface levels of receptors were assayed by addition of Alexa-647-conjugated M1 antibody (Sigma) for 45 minutes, as described previously (23). Fluorescence intensity profiles of cells populations (>5000 cells) were measured using a FACS-Calibur instrument (BD Biosciences). Each condition was performed in duplicate. Internalization was calculated by measuring the fraction of surface fluorescence remaining after 30 minutes of 1  $\mu\text{M}$  SKF81297 (Tocris) and divided by the non-treated condition.

### Luminescence-based cAMP assay

Experiments were conducted as previously described (23). Briefly, cells were transfected with the cyclic-permuted luciferase pGLOSensor-20F plasmid (Promega) and then treated with luciferin (GoldBio) in phenol and serum free media for 1 hour in a 24 well dish. Luminescence values for SKF81297 (Tocris) treated conditions were measured at their peaks and normalized with reference to 10  $\mu$ M forskolin (Sigma) at its peak.

### Total Internal Reflection Fluorescence Microscopy (TIRF-FM) Live Imaging.

Live cell TIRF-FM was conducted with a Nikon Ti-E inverted microscope at 37°C in a controlled humidity and CO<sub>2</sub> controlled chamber as described previously (23). D1 specific agonist SKF81297 (Tocris) was added at 1  $\mu$ M while D1 antagonist SCH23390 (Tocris) was added at 10  $\mu$ M.

### Preparation and transfection of cortical organotypic slice cultures

Rat hippocampal slice cultures were prepared from P6 – P7 pups as previously described (47, 48). pCMV-dLight1.2 (12 $\mu$ g) and pCMV-mCherry (3 $\mu$ g) were mixed with single cell electroporation solution (160 mM NaCl , 5.4 mM KCl, 12mM MgCl<sub>2</sub>, 2 mM CaCl<sub>2</sub> , 5 mM HEPES, pH 7.4 ) to total volume of 36  $\mu$ l. One-week old hippocampal cultured slices were transfected with single cell electroporation (49). 5 – 7 days after transfection, single hippocampal cultured slice was transferred to the imaging chamber in a custom built two-photon imaging setup. Slices were perfused in 10ml gassed artificial cerebral spinal fluid (ACSF) containing 4mM Ca<sup>2+</sup>, 4mM Mg<sup>2+</sup>, 0.5  $\mu$ M TTX and 10 $\mu$ M cocaine (DA transporter blocker) during imaging.

### AAV viral production

All dLight1 AAV constructs were cloned in the laboratory, and viruses were produced by the UC Davis Vision Center Vector Design and Packaging Core facility. The viral titers of the viruses used in this study were: AAV1.*CAG.flex.tdTomato*,  $\sim 8 \times 10^{12}$  genome copies (GC)/mL (University of Pennsylvania); AAV5.*hSynapsin1.flex.ChrimsonR.tdTomato*,  $\sim 4 \times 10^{12}$  GC/mL (University of North Carolina); AAV1. *hSynapsin1.NES-jRGECO1a*,  $\sim 3 \times 10^{13}$  GC/mL (University of Pennsylvania); AAV1. *hSynapsin1.dLight1.1*,  $\sim 1 \times 10^{12}$  GC/mL; AAV1. *hSynapsin1.dLight1.2*,  $\sim 2 \times 10^{12}$  GC/mL; AAV9. *hSynapsin1.dLight1.2*,  $\sim 4 \times 10^{12}$  GC/mL; AAV9.*CAG.dLight1.1*,  $\sim 7 \times 10^{11}$  GC/mL; AAV9.*CAG.control\_sensor*,  $\sim 1 \times 10^{12}$  GC/mL.

### Animals

Animal studies were conducted in compliance with the Guide for the Care and Use of Laboratory Animals of the National Institutes of Health and approved by the Institutional Animal Care and Use Committee (IACUC) at the University of California, Davis or the relevant institutional regulatory body. Wild type rats were used in this study (0-2 months old) for neuronal and organotypic slice culture preparation and two-photon imaging in brain slice. Dopamine receptor-D1 (*Drd1*)-Cre mice (4-6 months old, Jackson Labs, Strain B6; 129-Tg(*Drd1-cre*)120Mxu/MMJax) were used for two-photon imaging in the dorsal striatum. Vesicular GABA transporter (VGAT)::IRES-Cre (*50*) (Jackson Labs, Slc32a1tm2(cre)Lowl/J) and Tyrosine hydroxylase (TH)::IRES-Cre (*51*) (Jackson Labs, B6.129X1-Thtm1(cre)Te/Kieg) knock-in mice between 3 and 5 months old were used for in vivo imaging using fiber photometry and for optogenetic manipulations. Wild type male mice (2 to 5 months old, C57BL6/J, Jackson Laboratories) were used for two-photon in vivo imaging in the cortex. Sample sizes (number of

mice) for each experiment are stated in main text. All animals were group housed in standard plastic cages on a 12-hour light/dark cycle with food and water available *ad libitum*, except for mice trained on the visuomotor association task (see below). These mice were house individually on a reverse 12-hour light/dark cycle. Anesthesia was performed with 4.5% isoflurane for induction and 2% for maintenance.

### Viral injections

Injection procedures were essentially identical to those described in (10, 52-54) with a few exceptions.

For dopamine imaging in brain slice, male and female Sprague-Dawley rats (p23-27) were used for intracerebral microinjections. Briefly, anesthetized rats were immobilized in a Stereotaxic Alignment System (Kopf Instruments). AAV1.*hSynapsin1*.dLight1.2 (200 nl) was injected uni-laterally into the dorsal striatum using the following coordinates from bregma (in mm): 0.48 anteroposterior (AP),  $\pm 2.19$  mediolateral (ML), 4.69 dorsoventral (DV).

For dopamine imaging in the dorsal striatum, mice were injected in the dorsal striatum at two caudal locations (+0.6 and +0.2 AP and 2.1mm ML to bregma) and 3 depths below the surface (-1.6mm, -1.9mm, and -2.2mm; 100 nL at each depth, total 0.6uL) with either AAV1.*hSynapsin1*.dLight1.1 or AAV1.*hSynapsin1*.dLight1.2 in combination with AAV1.*CAG.flex.tdTomato* (diluted 1:100 in PBS). The flex-tdTomato in our experiments is expressed in roughly half of the SPNs (Drd1-cre mice) to avoid potential issues, such as competition of expression when two AAVs are co-expressed in the same neurons.

For dopamine imaging using fiber photometry, AAV9.*CAG*.dLight1.1 or AAV9.*CAG*.control\_sensor were injected into the NAc (+1.3 mm AP, -1.25 mm ML, -4.25

mm DV) and cre-dependent AAV encoding ChrimsonR-tdTomato was injected into the VTA (-3.3 mm AP, -0.5 mm ML, -4.3 mm DV). For dual color photometry experiments, AAV encoding jRGECO1a was 1:1 mixed with dLight1.1 virus and injected into the NAc region (+1.3 mm AP, -1.5 mm ML, -4.25 mm DV). A 10  $\mu$ L NanoFil microsyringe (World Precision Instruments) with a blunt 35-gauge needle was used for viral injection and manipulated by a microsyringe pump (UMP3, World Precision Instruments) and a controller (Micro4, World Precision Instruments). 500 nL of AAV was slowly injected into the target coordinates over 10 minutes, and additional 10 minutes were waited to allow diffusion. The needle was slowly withdrawn over 10-15 minutes.

For dopamine imaging in the cortex, anesthetized animals (4% isoflurane for induction; ~1.5% during surgery) were positioned in a computer-assisted stereotactic frame with digital coordinate readout and atlas targeting (Angle Two, Leica Biosystems Inc., Buffalo Grove, IL). Micropipettes were loaded with virus solution and slowly lowered into the brain under a ~32° injection angle until the target depth (~0.2 mm) was reached. Manual pressure was applied to a 30 mL syringe connected to the injection pipette. Virus solution was slowly injected over a period of 5–10 min. Once desired injection volume (200-400 nl) was delivered, the syringe's pressure valve was locked and position maintained for approximately 10 min to allow virus to spread and to avoid backflow upon needle retraction. Each mouse received two injections of AAV9. *hSynapsin1*.dLight1.2 (1:50 dilution). Injection coordinates were (AP 3-3.2 mm, ML 1-1.2 mm) and (AP 1.5 mm, ML 1-1.5 mm).

### Slice preparation

5% isoflurane was used to deeply anesthetize rats prior to decapitation. Brains were rapidly removed and placed in modified Krebs buffer containing (in mM) 126 NaCl, 2.5 KCl, 1.2 MgCl<sub>2</sub>, 2.4 CaCl<sub>2</sub>, 1.4 NaH<sub>2</sub>PO<sub>4</sub>, 25 NaHCO<sub>3</sub>, 11 D-glucose, and with 10 μM MK-801. Horizontal slices (245 μm) were taken using a Leica vibratome and allowed to recover for at least 30 minutes prior to use in Krebs with MK-801 being continuously bubbled with 95/5% O<sub>2</sub>/CO<sub>2</sub>. Slicing and recovery was done at elevated temperatures (30-34° C). Following recovery, slices were secured in a recording chamber maintained at 34° C and perfused with modified Krebs at a rate of 3 ml/min.

### Surgical procedures for in vivo imaging

#### Cannula implant for in vivo imaging in dorsal striatum

Two weeks post-injection, a chronic imaging window was implanted over the external capsule fibers above the striatal injection site as described previously (10). Briefly, a 2.75mm craniotomy was performed on anaesthetized mice, and cortical tissue was slowly aspirated until the white matter of the external capsule was exposed. A thin layer of Kwik-Sil (WPI) was applied over the imaging region, and a metal cannula covered at one end by a glass coverslip was inserted into the aspiration site down to the fiber surface.

#### Optical fiber implantation for fiber photometry and optogenetics

Mice were anesthetized with isoflurane and carbogen mixture (4-5% for induction, 1.5-2% for maintenance) and carefully placed to a stereotaxic frame (Kopf Instruments) after shaving their hair. Head skin was sterilized with chlorohexidine and a midline incision was

made using a sterile scalpel. The skull surface was exposed and cleaned with sterilized cotton swabs. Bregma and lambda points were identified and leveled to be at the same dorsal-ventral axis. Small craniotomy holes were made with drill bits (#73 size, Kyocera) over the nucleus accumbens (NAc) and ventral tegmental area (VTA). After viral delivery, optical ferrule/fiber (for VTA/optogenetics, 300  $\mu\text{m}$  diameter, 5-6 mm cut length, NA 0.37, home-made; for NAc/photometry, 400  $\mu\text{m}$  diameter, 5 mm cut length, NA 0.48, Doric lenses) was mounted to a stereotaxic cannula holder (Doric lenses). First, a 400  $\mu\text{m}$  fiber was lowered to the NAc through a craniotomy hole and stopped at 200  $\mu\text{m}$  above the virus injection target. A layer of adhesive cement (C&B Metabond, Parkell Inc.) was applied to the anterior portion of skull surface to strongly hold the implanted ferrule. Care was taken not to apply Metabond near the posterior craniotomy sites for VTA. Next, a 300  $\mu\text{m}$  fiber was inserted to the VTA and stopped at 500  $\mu\text{m}$  above the injection site. Another layer of adhesive cement was applied to hold the second fiber. After adhesive cement was fully dried, a thick layer of dental cement (Lang Dental) was applied to build a head cap.

#### Head plate and cranial window implantation for in vivo imaging in the cortex.

A few weeks after viral injections, mice were implanted with a head plate and cranial window on a custom surgical bed (Thorlabs Inc., Newton, NJ). Body temperature was maintained at 36–37 °C with a DC temperature control system and ophthalmic ointment was used to prevent eyes from drying. Skin was cleaned and disinfected with 70% ethanol and Betadine. A small (~10 mm) incision was performed along the midline. The scalp was pulled open and periosteum cleaned. First, a portion of the scalp was surgically removed to expose frontal, parietal, and interparietal skull segments. Then, the metal plate was affixed to the

bone with C&B Metabond Quick Adhesive Cement (Parkell Inc., Edgewood, NY). Next, to enable chronic two-photon imaging, a custom-made cranial window was implanted, similar to (55). The craniotomy (2.5 mm diameter) was centered around (AP 2 mm and ML 1.5 mm) and sealed with a custom three-layered cover glass assembly (each No.1 thickness) with the two layers closest to the cortex consisting of two pieces of circular 2.5 mm-diameter cover glass and the outermost layer consisting of a circular 4 mm-diameter cover glass that rested on the thinned skull. The dura mater was kept intact.

### Behavioral experiments

#### Sucrose consumption

Mice were handled daily for 5-10 minutes to reduce anxiety associated with experimenter's handling. Following recovery from surgery (~7 days) mice were water-restricted to 1.5 mL per day and maintained at 85-90 % of ad libitum weight. All behavioral experiments were carried out in an operant chamber within a sound-attenuating box (Lafayette Instruments). Behavioral tasks were implemented and controlled by ABET II software (Lafayette Instruments). TTL pulses were used to synchronize with fiber photometry recordings. After at least 7 days of water deprivation, mice were introduced to an operant chamber and allowed to freely explore with a patch cord connected. 50  $\mu$ L of 5 % sucrose water was delivered every 60 seconds (total 10 times) so that mice can learn the position of a lick port. Lick was detected as a break of infrared beam at the lick port. This habituation session was repeated two to three times for each mouse until they showed robust lick activity (>400 licks per session). At the recording day, mice underwent the same sessions while

recording dLight1 fluorescence with fiber photometry. For analysis, mean fluorescence values were obtained from baseline (-10~-5 s from lick onset) and during consumption (0~5 s).

#### Unpredictable footshock delivery

Mice were placed into an operating chamber with a patch cord connected for photometric recordings. Five electric footshocks (0.6 mA for 1 second) were delivered with variable intervals (randomly chosen from uniform distribution between 45 and 75 seconds) without predictive cues. This was performed after all other experiments, since such aversive stimuli can induce sustained fear and anxiety to the context. For analysis, mean fluorescence values were obtained from baseline (-5~-1 s from lick onset) and during footshock (0~2 s).

#### Cue-reward learning and extinction

In cue-reward learning sessions, CS was turned on for 10 seconds and US was available 7 seconds after CS onset, after variable inter-trial intervals (ITI). In cue-reward extinction sessions, same CS was turned on for 10 seconds without US delivery after variable ITI.

In “expected reward delivery” trials, US was delivered after CS presentation, as in previous learning sessions.

After sucrose consumption experiments, mice started appetitive Pavlovian conditioning, or cue-reward learning, in the same operant chamber. Conditioned stimuli (CS) consisted of house-light and 70 dB 5kHz tone, and were turned on for 10 seconds with variable intervals (randomly drawn from uniform distribution between 75 and 105 seconds). Unconditioned stimulus (US) was 50  $\mu$ L of 5 % sucrose water, available at the 7th second after each CS onset. Pump sound from liquid dispenser was audible from 6th to 7th seconds.

CS-US pairings were repeated 20 times per session (therefore ~30 minutes for each session). Mice underwent total of 12 sessions for cue-reward learning. Chambers and lick port were sanitized with Accel and 70% ethanol between animals to remove any odor. For all sessions, lick data and photometry recordings were simultaneously obtained. Two to three days after the last cue-reward learning sessions mice began cue-reward extinction. Identical CS were given 30 times per session with variable intervals (between 45 and 75 seconds), now without US delivery. Mice underwent total of 5 extinction sessions. To quantify CS-triggered behavior, number of licks was counted during CS presentation. For photometry data, peak fluorescence was obtained for CS (0~3 s after CS onset) and US (-2~5 s around US consumption onset). US consumption onset for each trial was defined as the lick bout onset after US is available, where lick bout onset was detected with a threshold of 2 Hz. To examine fluorescence response shift from US to CS (or vice versa), we calculated CS-US index, defined as  $(\text{CS response} - \text{US response}) / (\text{CS response} + \text{US response})$ .

#### Unexpected reward delivery and omission

After 12 cue-reward learning sessions, mice underwent reward prediction error experiments. In “unexpected reward delivery” session, animals were exposed to normal CS-US pairing trials; but in 25% of trials, US was delivered without CS, so that mice can explore to the lick port without predictive cues and consume reward in an unexpected manner. Peak fluorescence values after US consumption onset was obtained and compared between expected and unexpected conditions. In “unexpected reward omission” sessions, US delivery was omitted in 4 out of 20 trials (4th, 8th, 13th, and 16th trials) after predictive CS onset. For

analysis, mean fluorescence values were obtained from baseline (-10~0 s from CS onset) and after CS offset (10.5~11.5 s) and compared.

### Visuomotor learning task

Prior to surgical preparation and behavioral training, mice were handled/tamed on two consecutive days to reduce stress during experiments. Following recovery from surgery (~7 days) mice were water-restricted to 25 ml kg<sup>-1</sup> per day and maintained at 80-85% of ad libitum weight. Training was performed in a custom-built setup that included a color LCD monitor (12.1" LCD Display Kit/500cd/VGA, ICP Deutschland GmbH) on which visual stimuli were presented. To reduce noise in optical recordings, the monitor was covered with a color filter (R342 Rose Pink, Rosco Laboratories Inc.). During training, mice were head-fixed with a custom-build head holder and placed on a spherical treadmill (Habitrail Mini Exercise Ball, Animal World Network) facing the LCD display. An optical encoder (E7P OEM, US Digital) attached to the treadmill allowed measurement of both speed and direction of ball movement. Water reward was delivered with a programmable syringe pump (NE-500 OEM Syringe Pump, New Era Pump Systems, Inc.). Behavioral signals were acquired through a data acquisition board (PCI-6221, National Instruments) connected to a breakout box (BNC-2110, National Instruments) and interfaced to MATLAB using the Data Acquisition Toolbox (Version R2010bSP2, The MathWorks Inc.). Behavioral task sequence was controlled by the MATLAB-based software MonkeyLogic ([www.monkeylogic.net](http://www.monkeylogic.net)) (56, 57). Custom-written functions were added to MonkeyLogic to enable analysis and control of ball rotation parameters. Treadmill encoder signals, trial marker codes (generated by MonkeyLogic), and imaging data were acquired in synchrony allowing running parameters, behavioral task events, and image frames to

be linked.

Once the mouse stopped moving on the ball, a sequence of task events was initiated. First, a blue square frame was displayed on the monitor and required the animal to continue to stand still for a period of 10 s (ball rotation/velocity  $\leq 2$  mm/s). If the mouse continued to stand still for the entire stand-still phase, a second stimulus, a filled blue square, was presented for 3 s, instructing the mouse to initiate a run. If the mouse initiated sustained movement (ball rotation/velocity  $>10$  mm/s for  $>1$ s duration) during the 3s stimulus phase, a water reward was delivered. In 20% of pseudo-randomly selected trials the reward was withheld (“Unexpected reward omissions”; light green traces in Fig. 5, fig. S15 and S16). If no running occurred, the trials counted as a miss trial. If the animal began to move during the 10 s stand-still phase (ball rotation/velocity  $> 2$  mm/s), the trial was aborted and no water reward was delivered (“Spontaneous run trials”; pink traces). The mouse was able to initiate a new trial after an intertrial interval (ITI) of 5 s.

During the first two days of training, mice spent  $\sim 15$ -30 min/day in the setup to become accustomed to head restraint. Mice were then trained daily for 60-90 min during which they performed  $\sim 300$ -700 trials. Task parameters were adjusted depending on individual animal’s performance. Initially, the duration of the stand-still phase was set to 3 s, the stimulus phase to 20 s, and the running threshold to 2 mm/s. This increased the chance for the mouse to receive the task-dependent reward. The stand-still phase was then progressively extended and the stimulus phase shortened to establish the association between stimulus onset and running onset. Training continued until median reaction times (RT) had dropped below 1500 ms, which indicated that mice had learned to associate the visual cues with the desired behavior. Task proficiency was typically reached within 5-7 days. During the initial training phase all successful “Go” trials

were rewarded. Unexpected reward omission trials were introduced during imaging sessions only.

### In vivo optogenetic and pharmacological manipulations

For optogenetic experiments, a patch cord (1 m length, 1.25 mm zirconia ferrule, 300  $\mu$ m diameter fiber, Doric lenses) was used to connect to a ferrule on an animal's head cap and a swivel commutator (fiber-optic rotary joints, Doric lenses) to allow free movement. Another patch cord was connected from the commutator and to a 635 nm diode-pumped solid-state laser (Changchun New Industries Optoelectronics Technology). The intensity of laser was measured with a power meter (PM100D, Thorlabs) and calibrated to be 10 mW at the fiber tip. An external TTL pulse generator (OTPG4, Doric Lenses) was used to control the laser output. For activating VTA DA neurons, 5 Hz, 10 Hz, and 20 Hz of 10 ms pulses were applied for 2 seconds. For activating VTA GABA neurons, 40 Hz pulses were used (58). These pulse trains were repeated 40 times per animal with intervals of 30 seconds. For pharmacological manipulations, the following drugs were used: DRD1 antagonist (SCH-23390, 0.25 mg/kg) and selective DA reuptake inhibitor (GBR-12909, 10 mg/kg) (59). Animals were injected with these drugs or saline (0.9% sodium chloride) through intraperitoneal delivery 30 minutes before optogenetics/photometry experiments. Mean or peak fluorescence values were obtained before (-5~-1 s from onset), during (0.5~2 s) or after (4~10 s) photoactivation.

## Data acquisition and analysis for ex vivo and in vivo imaging

### Ex vivo imaging in rat brain slice

Imaging was carried out in a custom built 2-photon microscope. Data were acquired and collected using ScanImage software (60). Slices were scanned at different frequencies, depending on the experiment, using 920 nm light. Electrical stimulation through a glass monopolar electrode placed within the slice near the area of imaging was used to evoke dopamine release. Experiments were carried out with a scan rate of 2 (128x128 pixels) or 15 (32x32 pixels) Hz. The fluorescence over the entire field (20x20  $\mu\text{m}$ ) was measured for each frame and plotted against time. Drugs were applied by superfusion. Line scans were taken at a 500 Hz frame rate. To measure the dopamine response curve, two-photon images were taken every minute. Image analysis was performed using custom software written in MATLAB.

### In vivo imaging in mouse dorsal striatum

Treadmill velocity and acceleration were sampled at 1000Hz by a rotary encoder (E2-5000, US Digital) attached to the axle of the treadmill. Two-photon imaging was performed as described previously (61), using the same collection optics, but without the electric lens. 920 nm laser light was used for excitation and 1024x512 pixels time series datasets were acquired at 30 Hz. Imaging sessions began after mice were acclimated to head fixation and ran frequently on the treadmill (~1-3 days). Imaging data was collected over 1-2 days from dorsal striatum fields ranging from 250 to 450 $\mu\text{m}$  in diameter. All analyses were carried out using custom software written in MATLAB. Time series movies were motion corrected on the static red channel using algorithms described previously (62) and x and y shifts from the red were used to correct the green channel. Mean whole field fluorescence was calculated from a large, hand-selected ROI

containing all regions of the field with visible cellular structure in the red td-Tomato channel. Fluorescence time series were converted to  $\Delta F/F$  by normalizing signals to an 8th percentile baseline (62) within a sliding window ( $\pm 15$ s around each point) to correct for slow drift and bleaching. Significant positive-going transients were calculated as previously described (62).

### In vivo imaging with fiber photometry

Fiber photometry was performed as in (28, 63, 64). For dual color imaging a three LED system was used (FMC7, Doric Lenses): 490 nm for dLight1, 565 nm for jRGECO1a, and 405 nm to be used as isosbestic wavelength for both indicators. The following dichroic filters and excitation/emission filters were used (all from Semrock): Di02-R405, Di02-R442, FF495-Di03, FF552-Di02, FF593-Di03, FF01-405/10, FF01-433/24, FF01-475/28, FF02-520/28, FF01-565/24 and FF02-641/75 (28, 63, 64). Acquired photometry data were processed with custom-written codes in MATLAB. Raw data from each channel were low-pass filtered at 25 Hz (for single color imaging) or 12 Hz (for dual color imaging) using a 2nd order Butterworth filter with zero-phase distortion. To calculate  $\Delta F/F$  time series, a linear fit was applied to the 405 nm signals and aligned to the 490 and 565 nm signals. The fitted 405 nm signal was subtracted from 490 and 565 nm channels, and then divided by the fitted 405 nm signal to yield  $\Delta F/F$  values. Dual color imaging data were down-sampled to 100 Hz. In Pavlovian conditioning,  $\Delta F/F$  time-series signal is further normalized using robust Z-score (subtraction of median and division by median absolute deviation, calculated from the entire session) to account for potential differences in signal variance across animals and sessions. Photometry signals were then extracted around relevant behavioral events (e.g. lick onset, footshock delivery, CS onset) and averaged. Power spectral density was estimated for averaged

dLight1/control sensor fluorescence data upon optogenetic stimulation of different frequencies. We used Welch's method with 2-second window size and 50% overlap to estimate power from 0.5 to 25 Hz in 0.1 Hz step.

#### In vivo two-photon imaging in the cortex.

Once mice had reached proficiency on the task, they were imaged daily for up to 9 days. Imaging was performed using a resonant scanning two-photon microscope (Sutter Instrument) equipped with a pulsed femtosecond Ti:Sapphire laser (Chameleon Ultra II, Coherent). dLight1 fluorescence was excited with 910 nm light, and detected using a ET525/70M emission filter (Chroma Technology Corp.) and H7422-40 GaAsP photomultiplier tube (Hamamatsu Photonics). Average excitation power was 40-130 mW depending on imaging depth and dLight1 expression levels/duration. Typical recording depth was 80-150  $\mu\text{m}$  below the pia. Data were acquired using a Nikon 16x 0.8-NA water immersion objective. A custom-made blackout curtain around the microscope's detector was used to reduce light contamination by the LCD monitor. Images (512 $\times$ 512 pixels) were acquired at 30.8 frames/sec. Recording sessions consisted of five to twelve  $\sim$ 10 min recordings, separated by short imaging breaks (3-5 min). Recordings within a given session were performed at the exact same location to maximize the number of trial repetitions for analysis. Recordings from different sessions were performed at the same injection sites but offset either laterally or axially to maximize tissue volume being sampled.

#### Analysis of cortical in vivo imaging data

All data were analyzed using custom code written in MATLAB (MathWorks). Data from four animals were included in the analysis. Mouse #1 underwent 4 recording sessions starting 8

weeks after virus injection. Mouse #2 underwent 9 recording sessions starting 3 weeks after injection. Mouse #3 underwent 2 recording sessions starting 2 weeks after injection and Mouse #4 underwent 4 recording sessions starting 6 weeks after injection. Recording locations (M1/M2/FrA) are indicated in fig. S16E.

To confirm the animals' responsiveness to the "Go" stimulus, we compared proportions of trials in which runs were triggered by "Go" stimulus presentation ("Hit trials") and proportions of trials in which no such response occurred ("Miss trials") (fig. S16A and C). A steep increase in "Miss trials" at the end of the session indicated that mice had lost interest in the water reward. Trials beyond that point (black vertical line in fig. S16A) were excluded from analysis. To confirm that mice had learned the task, we analyzed the animals' RTs (defined as the time interval between "Go" stimulus onset and movement onset/ball velocity >10 mm/s) (fig. S16B and D). RTs below 1500 ms indicated that mice had learned to associate the visual cues with the desired behavior.

To reduce random noise in our time-lapse recordings a sliding average filter was applied (8 frames or 260 ms). This filtering largely retained the temporal dynamics of dLight1 fluorescence signals. Lateral image motion (e.g., due to mouse movement) was corrected using a cross-correlation registration algorithm, with an average image of 50 consecutive frames from the time-lapse recording serving as the reference image. The same reference image was used to correct image motion of other recordings from the same location. Noise in motion-corrected image data was further reduced using a Kalman filter.

To quantify/classify dLight1 transients, we tiled the field of view (FOV) with equally sized (~17x17 $\mu$ m) regions of interest (ROIs). To exclude ROIs with little or no dLight1 expression (e.g., on blood vessels) we first generated a mean fluorescence projection image from

the corresponding time-lapse recording. We then calculated the projection image's pixel intensity distribution. ROIs with mean pixel intensity values below the 55<sup>th</sup> percentile of this distribution were excluded from analysis. To extract fluorescence time traces  $F(t)$  from all remaining ROIs, pixel intensities of each ROI were averaged.  $\Delta F(t)/F$  was calculated as  $(F(t) - \text{mean } F) / \text{mean } F$ . ROIs that showed transients with negative amplitudes (predominantly located near blood vessels) were excluded from further analysis.

Each ROI's time trace included multiple trials/task repetitions. Based on the animal's performance on the trials, time traces were subdivided into "Expected reward", "Unexpected reward omission", and "Spontaneous run" trial traces. This was done for all recordings from the same location using the same ROIs. Extracted trial traces were then sorted by trial type, aligned to running onset, and averaged (fig. S16G, single ROIs). To ensure that cued and spontaneous running bouts were comparable, only traces from spontaneous runs starting  $> 5$  s after stand-still cue onset and with  $> 5$  mm/s ball rotation/velocity were included. To calculate population responses, "Expected reward", "Unexpected reward omission", and "Spontaneous run" trial traces from all animals, all sessions, and all significant ROIs were averaged (Fig. 5E, group average).

To identify ROIs with significant increases in dLight1 fluorescence in response to the task, three analysis intervals were defined (fig. S15A): (I) Baseline (from -7 to -2 s prior to run onset), (II) reward expectation (from run onset to 3.3 s after run onset), and (III) reward interval (from 4.3 s to 10.8 s after run onset).  $\Delta F/F$  traces for each trial were averaged during the three trial intervals respectively. The distributions of the averaged  $\Delta F/F$  traces for particular trial types were then statistically compared among each other and between intervals. ROIs that showed significant fluorescence increases during the reward expectation but not the reward interval, and

for all trial types compared to the baseline interval, were defined as “ROI active during locomotion” (white squares in Fig. 5 and fig. S16G). ROIs that showed significant fluorescence increases during the reward expectation but not reward interval for cued/triggered but not spontaneous run trials were classified as “ROI active during reward expectation” (black squares). Finally, ROIs that showed significant fluorescence increases during the reward interval for rewarded but not un-rewarded or spontaneous run trials were defined as “ROI active during reward” (red squares). Significance was determined using the Wilcoxon’s rank-sum test ( $p < 0.05$ ), Bonferroni corrected for multiple comparisons.

All ROI analysis was performed on motion corrected image data (see above) averaged across trials of the same type and from the same session. To investigate whether this averaging introduces artifacts in the DA transients (e.g., due to stereotypic running-related image movements) we inspected our data more closely at cellular and population levels. Close observation of a 40x45 pixel detail of the motion corrected image data revealed stable and sharp images even during the most vigorous running periods (fig. S15A). Next, we plotted the full field of view (FOV) intensity changes for the average data of each trial type aligned at run onset (fig. S15B). This revealed that the main characteristics of the single ROI transients are retained in the full FOV average, arguing against a pronounced contamination by motion artifacts. Next, to investigate residual lateral shifts in the average image data for each trial type, we applied our motion correction algorithm. The detected residual image motion was  $< 2$  pixels for all sessions and mice (fig. S15C and D). To verify that our motion correction algorithm reliably detects sub- and supra-pixel image displacements we artificially introduced random lateral shifts of up to 5 pixels to the same average image data (fig. S15E). The error between the introduced shifts and the shifts detected by the algorithm across 100 repetitions was  $0.089 \pm 0.001$  pixels (mean  $\pm$

SEM). Together, this suggests that DA transients extracted from our 17x17 $\mu$ m ROIs are unlikely an artifact of image motion (fig. S15F).

### Histology

Histological verification of proper sensor expression was as described previously (64). Primary antibodies used were: chicken anti-GFP (1:500; GFP-1020, Aves Labs), chicken anti-TH (1:500; TYH, Aves Labs) and rabbit anti-RFP (1:500; 600-401-379, Rockland A&A).

### Hybrid chain reaction combined with immunohistochemistry

To assess the expression pattern of ChrimsonR-tdTomato injected into the VTA of VGAT::IRES-Cre mice, we performed combined in situ hybridization for labeling *vgat* mRNA and immunohistochemistry (IHC) for detecting DAergic neurons (with TH). To achieve high-sensitivity in situ hybridization of *vgat* in tissue slices, we used hybridization chain reaction (HCR) (65, 66). First, we designed 22 probes for targeting *vgat* using a custom written software (available at <https://github.com/GradinaruLab/HCRprobe>). Each probe consists of 20-nt target sequence, 2-nt spacer, and 18-nt initiator. We selected the target sequences that has (1) the GC content of 45-60%, (2) no nucleotide repeats more than 3, (3) no more than 20 hits when blasted, (4) higher than a  $\Delta G$  of -9 kcal/mol to avoid self-dimers. Then we blasted full sequences (target sequences with spacer and initiator) and calculate Smith-Waterman alignment scores between all possible pairs to exclude probes forming cross-dimers. The designed probes were synthesized by Integrated DNA Technologies.

HCR was performed on 50  $\mu$ m-thick slices and kept in RNAlater solution (ThermoFisher Scientific). Slices were permeabilized in PBST (1xPBS with 0.1% Triton X-100) for 1 hour at

room temperature (RT) and pre-hybridized in hybridization buffer (2x saline-sodium citrate (SSC) , 10% ethylene carbonate, 10% dextran sulfate) for another hour at 37°C. Then the samples were incubated in pre-warmed hybridization buffer including probes (2 nM for each) at 37°C overnight. After hybridization, we performed stringent washes with wash buffer (2xSSC, 10% ethylene carbonate) for 30 min at 37°C and washes with 2xSSC for 30 min at RT (twice for each). The amplification step was performed as described in (67) overnight.

For IHC labeling of TH on HCR-labeled tissue slices, we used IHC buffer consisting of 2xSSC, 1% donkey serum, and 0.1% Triton X-100. We incubated the samples in IHC buffer for 1 hour at RT for blocking and added primary antibody (anti-TH, AB152, Millipore, 1:200). Primary antibody reaction was performed for overnight at RT. Following the wash steps with 2xSSC at RT for 30 min twice, the samples were incubated in IHC buffer including secondary antibodies (1:200) for overnight at RT. The samples were rinsed with 2xSSC a few times and mounted on a glass slide with mounting media (Prolong Diamond, ThermoFisher Scientific).

### Probe sequences (5'→3')

1	CACTTCATATCACTCACTaaGACACGGAGGTGGCCACATT
2	CACTTCATATCACTCACTaaGCGATGCTCAAAGTCGAGAT
3	CACTTCATATCACTCACTaaCCTGAATGGCATTGTCACG
4	CACTTCATATCACTCACTaaACCAGGACTTCTGCGACACG
5	CACTTCATATCACTCACTaaTTCTTCAGGAAGGCGCAGGG
6	CACTTCATATCACTCACTaaTTCTCCAGGCCCAATCACG
7	CACTTCATATCACTCACTaaGTGTAGCTGAACACGATGAT
8	CACTTCATATCACTCACTaaGCGGCGATGTGTGTCCAGTT
9	CACTTCATATCACTCACTaaACTTCCTTGGTCTCGTCGGC
10	CACTTCATATCACTCACTaaCGCGAAGAAGGGCAACGGAT
11	CACTTCATATCACTCACTaaAGGCGCAAGTGAAGAGGCT
12	CCTTGGCCTGGGACTTGTTGaaCCCAATCTCTATCTACCC
13	ATGTCCATCTGCAGGCCCTGaaCCCAATCTCTATCTACCC

14	TAGGCCAGCACGAACATGCaaCCCAATCTCTATCTACCC
15	CACCGCTGTGGCTATGATGGaaCCCAATCTCTATCTACCC
16	ACTTGGACACGGCCTTGAGAAaCCCAATCTCTATCTACCC
17	CGTCGATGTAGAACTTACCaaCCCAATCTCTATCTACCC
18	AGGGCAGGAAGATCTGCGACaaCCCAATCTCTATCTACCC
19	AGAGACCCTTGAGCACGCAGaaCCCAATCTCTATCTACCC
20	CGGGCAGGTTATCCGTGATGaaCCCAATCTCTATCTACCC
21	TTCTCCAGCACTTCGACGGCaaCCCAATCTCTATCTACCC
22	ACAGCAGCTTGCGCCAGAGAAaCCCAATCTCTATCTACCC

### Statistical Analysis

All statistical analyses were performed in MATLAB (MathWorks), Igor Pro (WaveMetrics) or Prism (GraphPad). We used both parametric (t-test, one-way ANOVA, two-way ANOVA) and non-parametric (Wilcoxon's rank-sum) tests. Pearson's correlation coefficients and their p-values were calculated to assess how behavior or dLight1 fluorescence evolved across reward learning or extinction. All tests were two-tailed. Error bars are standard error of the mean or standard deviation as indicated in figure legends and main text. No statistical methods were used to predetermine sample size.



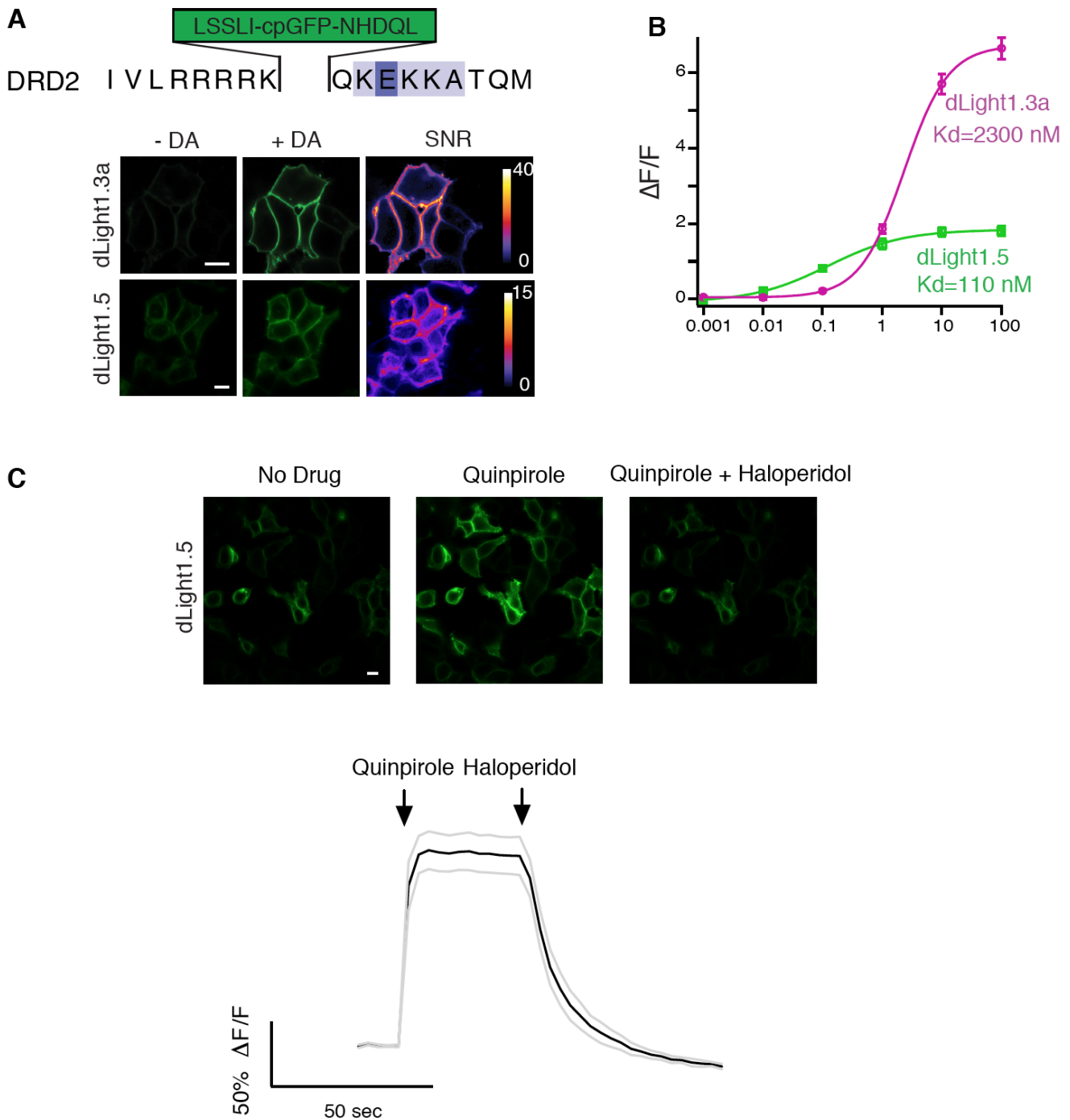
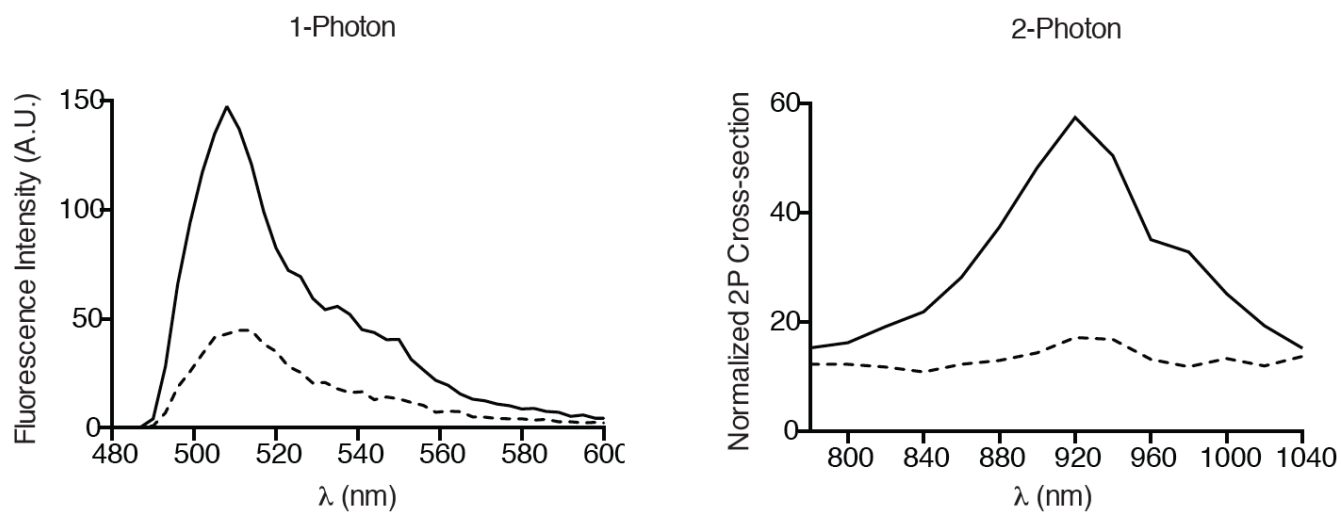


**Fig. S2. Characterization of dLight1.3a and dLight1.5.** (A) Top, amino acid sequence of DRD2 insertion site for the cpGFP module. Bottom, representative images of dLight1.3a and dLight1.5 expressed on HEK293 cells before and after addition of DA (10  $\mu$ M) and corresponding SNR heatmaps. Scale bars, 10  $\mu$ m. (B) Quantification of fluorescence response of dLight1.3a (n=12) and dLight1.5 (n=4) to DA titrations on HEK293 cells. Data were fit with Hill equation (EC50: dLight1.3a, 2300  $\pm$  20 nM; dLight1.5, 110  $\pm$  10 nM). (C) Representative images of dLight1.5 under basal conditions, after addition of quinpirole (10  $\mu$ M) and haloperidol (50  $\mu$ M), and trace showing quantification of fluorescence response during bath application of drugs (n=15). All data are shown as mean  $\pm$  SEM.

### dLight1.1



### dLight1.2

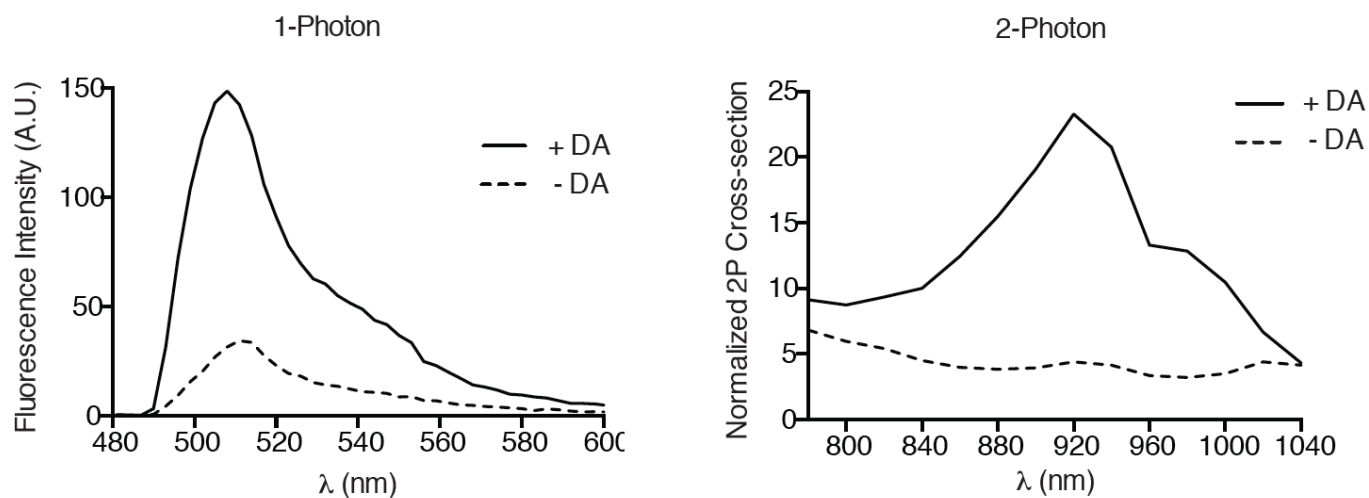


**Fig. S3. One photon emission spectrum and two-photon cross-section of dLight1 expressed in HEK293T cells.** Emission spectrum of both dLight1.1 and dLight1.2 peaks at 517 nm. Under 2P illumination, emission peaks are driven at 920 nm.

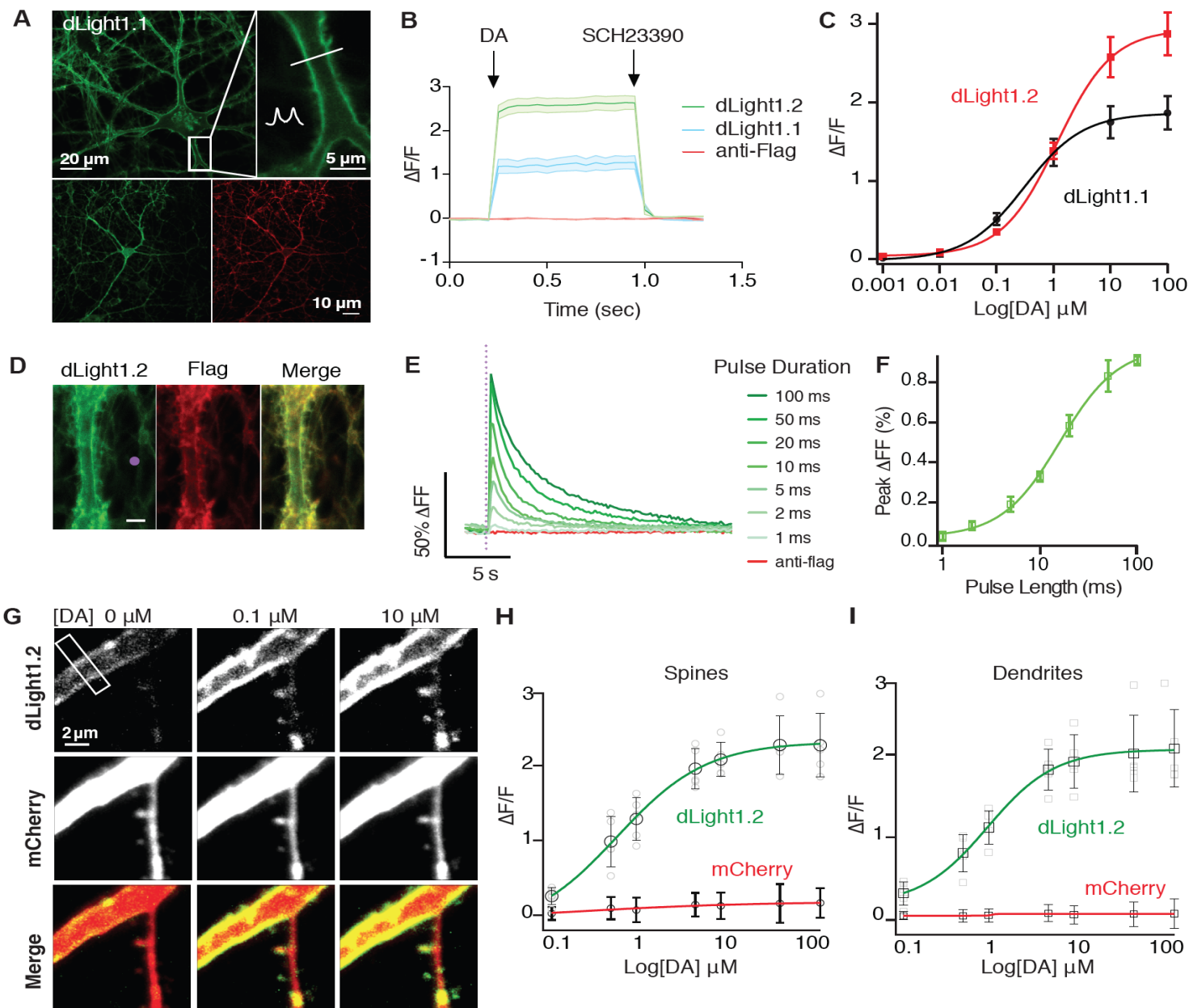


**Fig. S4. Characterization of dLight1 in cultured hippocampal neurons and organotypic hippocampal slice.** (A) Representative images showing membrane localization of dLight1.1 (GFP fluorescence in green, Alexa-564-conjugated anti-flag labeling in red) in cultured hippocampal neurons. Inset shows membrane intensity profile. (B) dLight1.1 and dLight1.2 responses to dopamine perfusion, which were abolished immediately with the addition of a DRD1 antagonist (mean  $\pm$  SEM,  $n=4$  sessions). (C) In situ titration on neurons (mean  $\pm$  SEM,  $n=7$  cells). Fitted with Hill equation ( $EC_{50}$ : dLight1.1,  $311 \pm 26$  nM; dLight1.2,  $1,157 \pm 44$  nM). (D) Representative images showing uncaging spots (purple circle,  $2 \mu\text{m}$  diameter, 40% laser power 405 nm light). Scale bar,  $5 \mu\text{m}$ . (E) Representative traces of dLight1.2 fluorescence in response to increasing duration of uncaging light pulses (1ms per pulse). (F) Quantification of peak  $\Delta F/F$  values which is correlated with the number of uncaging pulses (1 ms,  $2.7 \pm 0.01$  %; 2 ms,  $8.2 \pm 2.2$  %; 5 ms,  $18.9 \pm 3.9$ ; 10 ms,  $32.8 \pm 2.5$ ; 20 ms,  $58.4 \pm 5.3$ ; 50 ms,  $83.4 \pm 7.8$ ; 100 ms,  $91.1 \pm 6$  %;  $n=3$ , mean  $\pm$  s.d.). (G) Representative dLight1.2 responses to bath applied DA from sparsely-labeled CA1 pyramidal neurons in organotypic slice cultures. mCherry expression was used as a cell fill to visualize dendritic and synaptic structures (shown in rectangular and circular boxes, respectively) and to provide reference fluorescence. (H-I) Quantification of both green and red (control) fluorescence signal change at single spines and dendrites in response to a titration of DA concentrations. Maximal  $\Delta F/F\%$  fold change in the green channel were: synaptic spines,  $227 \pm 39$ ; dendrites  $201 \pm 46$  (mean  $\pm$  s.d.,  $n=5$ ).  $EC_{50}$  values were: spines,  $844$  nM; dendrites,  $883$  nM.

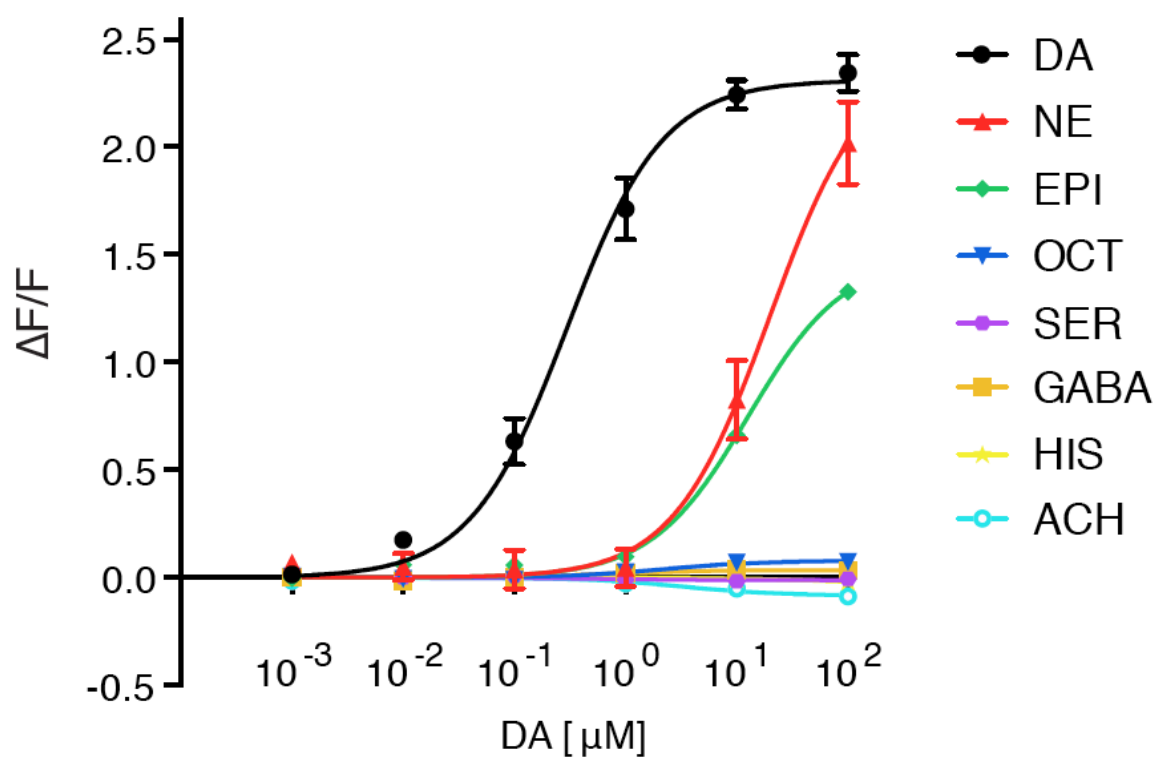


**Fig. S5. Specificity of dLight1.** Specificity of dLight1 response was determined by titrations of a panel of 8 different neuromodulators on dLight1.1-expressing HEK293 cells. Acetylcholine, ACH; histamine, HIS;  $\gamma$ -aminobutyric acid, GABA; serotonin, SER; octopamine, OCT; epinephrine, EPI; norepinephrine, NE; dopamine, DA.  $K_d$  values for DA, NE and EPI were:  $330 \pm 28$  nM,  $19,850 \pm 2,644$  nM,  $12,680 \pm 1,559$  nM, respectively. Results shown as mean  $\pm$  SEM, (n=3).

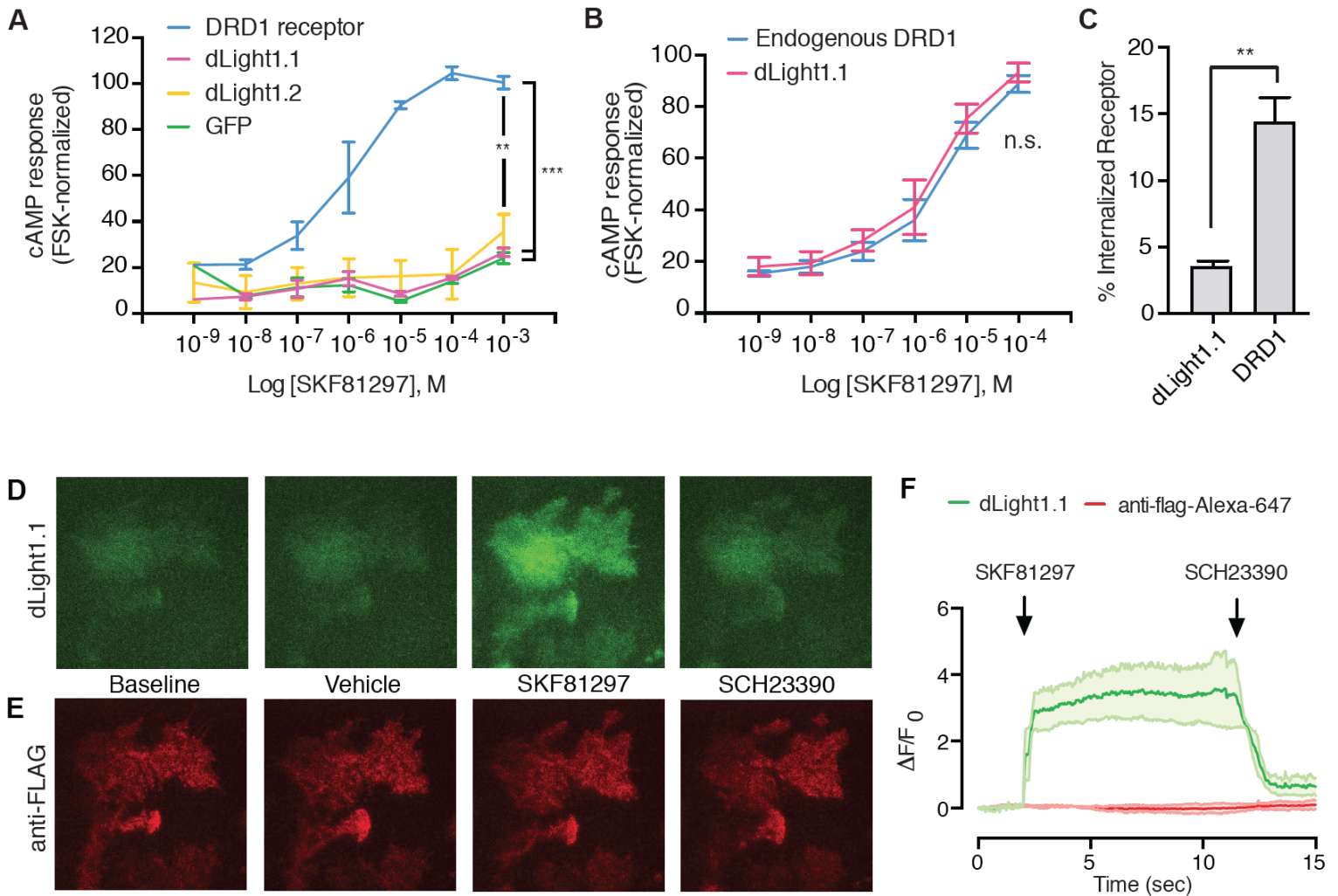


**Fig. S6. Functional analysis of dLight1 signaling properties.** (A) cAMP response curve to a titration of DA in HEK293T cells expressing wild-type human DRD1 receptor or dLight1.1 or dLight1.2 or GFP. No significant cAMP response were observed in cells expression dLight1.1 ( $n=3$ ,  $**p<0.01$ ,  $***p<0.001$ , one-way ANOVA, Dunnett's post test). (B) cAMP response curves of a cell line endogenously expressing DRD1 (U2OS). Overexpression of dLight1.1 did not alter the cAMP response to DA ( $n=3$ ,  $p=0.192$ , two-way ANOVA with Tukey's post-hoc test). (C) dLight1.1 internalization is significantly reduced compared to wild type DRD1 as assayed via flow cytometry (% internalized receptor: dLight1.1,  $3.4 \pm 0.5$  %; DRD1,  $14.3 \pm 1.9$  %;  $**p<0.01$ , unpaired t test). (D) TIRF microscopy visualization of dLight1.1 shows the fluorescent response to a DRD1 agonist (SKF81297) in green channel but not in red channel, which was immediately abolished by applying antagonist (SCH23390). (E) In situ surface staining with an Alexa-647 conjugated anti-flag antibody further confirmed the lack of internalized punctae. (F) Quantification of fluorescence responses in (D) and (E).

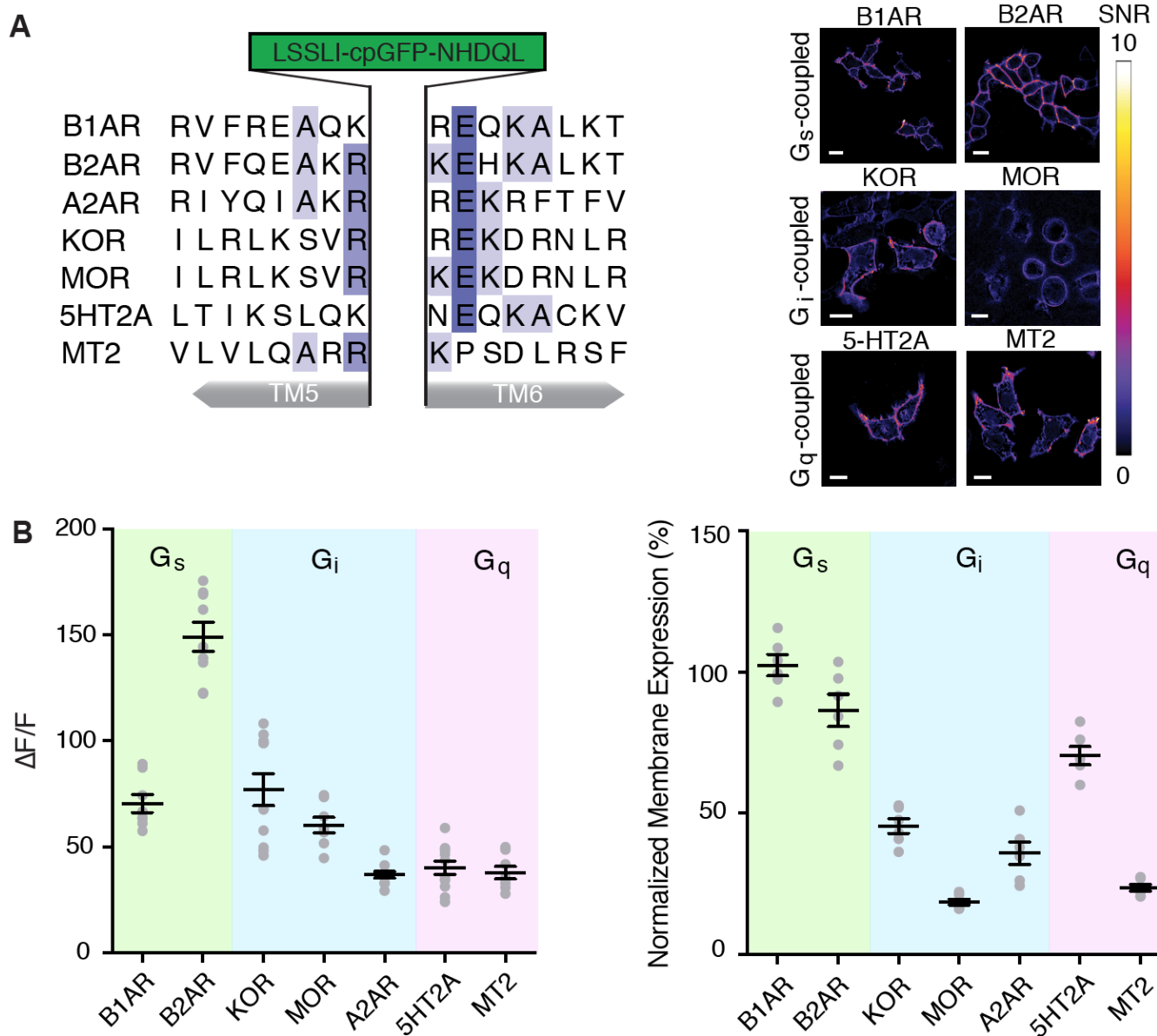


**Fig. S7. Versatility of engineering approach to generate other GPCR-sensors.** (A) Left, aligned sequences of TM 5 and TM6 from 7 GPCRs with insertion site for cpGFP module. To maximize  $\Delta F/F$  in the B2AR and MT2 constructs the “QLQKID” sequence was inserted between TM5 (after the last R) and before LSS. Scale bars: 10  $\mu\text{m}$ . Right, SNR heatmaps for a subset of GPCR sensors expressed in HEK cells. (B) Quantification of fluorescence response and membrane expression for each GPCR-sensor construct. Max  $\Delta F/F$  of each sensor to bath applied agonist (B1AR:  $70 \pm 4\%$ ,  $n=8$ ; B2AR:  $149 \pm 7\%$ ,  $n=9$ ; A2AR:  $77 \pm 8\%$ ,  $n=11$ ; KOR:  $60 \pm 4\%$ ,  $n=8$ ; MOR:  $37 \pm 2\%$ ,  $n=10$ ; 5HT2A:  $40 \pm 3\%$ ,  $n=12$ ; MT2:  $38 \pm 3\%$ ,  $n=8$ ). Agonists used were: norepinephrine for B1AR, B2AR, A2AR (100  $\mu\text{M}$ ); U50488 for KOR (10  $\mu\text{M}$ ); [D-Ala<sup>2</sup>, NMe-Phe<sup>4</sup>, Gly-ol<sup>5</sup>]-enkephalin (DAMGO) for MOR (10  $\mu\text{M}$ ); serotonin for 5HT2A (10  $\mu\text{M}$ ); melatonin for MT2 (10  $\mu\text{M}$ ). Membrane expression was calculated as membrane-to-cytosol ratio and normalized to dLight1.1 (B1AR,  $102 \pm 4\%$ ; B2AR,  $86 \pm 6\%$ ; DRD2,  $39 \pm 4\%$ ; A2AR,  $36 \pm 4\%$ ; KOR,  $45 \pm 3\%$ ; MOR,  $19 \pm 1\%$ ; 5HT2A,  $70 \pm 3\%$ ; MT2,  $24 \pm 1\%$ ;  $n=6$ ). Individual datapoints are shown. mean  $\pm$  SEM shown in black.

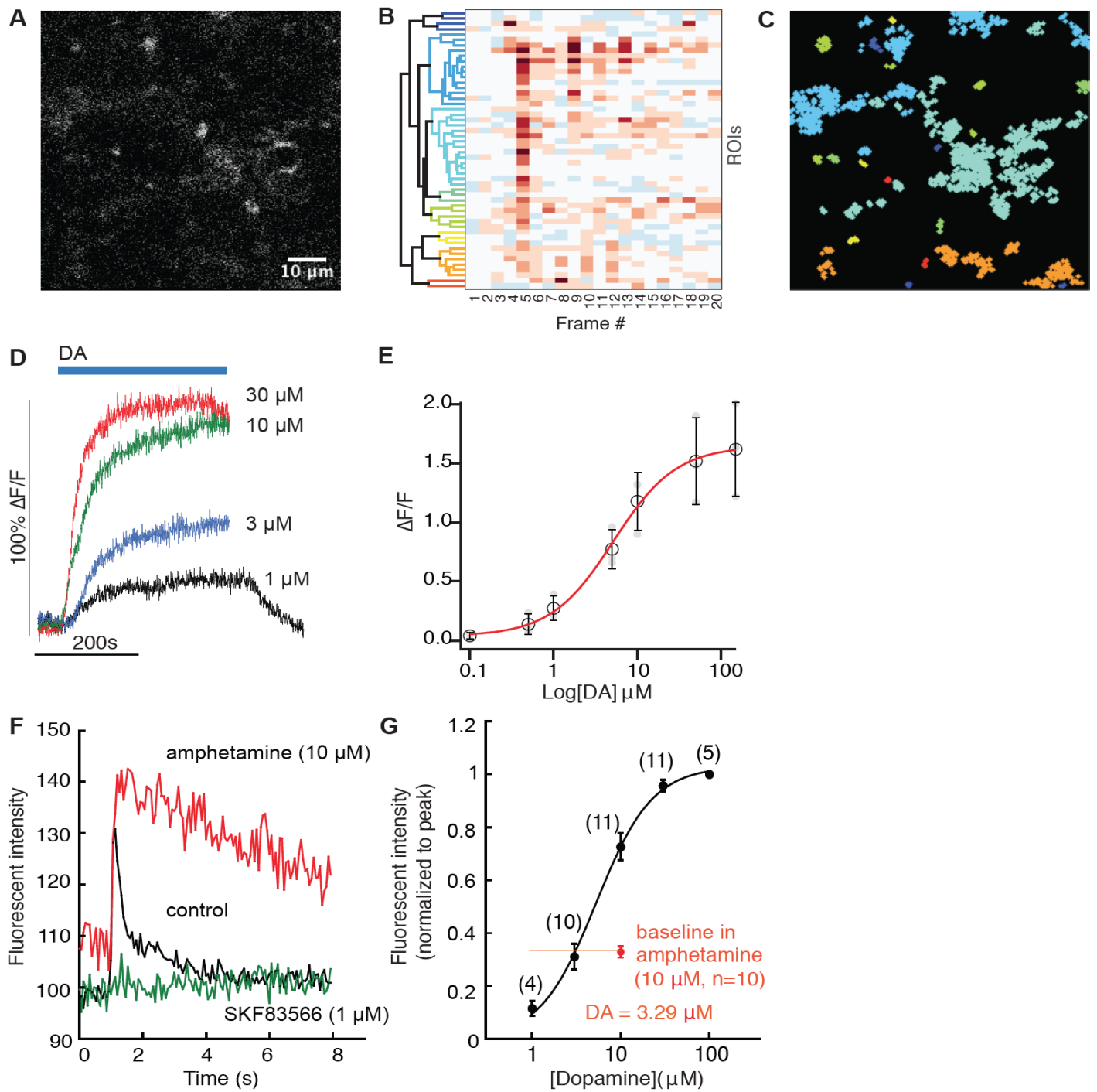


**Fig. S8. Characterization of dLight1 performance in striatal brain slice.** (A-C) Spatially-distinct responses triggered by electrical stimuli in acute rat striatum slice. (A) Representative field of view for two-photon imaging of acute striatum slice infected with AAV9.*hSynapsin1*.dLight1.2. (B) ROIs hierarchically clustered based on correlations in the time course of their fluorescence values. (C) ROIs location relative to (A), with color-coding corresponding to the dendrograms from the hierarchical clustering. (D) A steady-state concentration response curve with bath application of specified DA concentrations in the presence of cocaine (10  $\mu\text{M}$ ) and sulpiride (400  $\mu\text{M}$ ) to block D2-autoreceptors. The increase in fluorescence to each known concentration of DA (1-100  $\mu\text{M}$ ) was measured after reaching a steady level in 3-10 min. (E) Quantification of concentration-dependent fluorescence responses from (D). The fluorescence response reached half-maximal levels at about 5  $\mu\text{M}$  DA and approached saturation at 30-100  $\mu\text{M}$ . Curve was fitted with a Hill equation ( $\text{EC}_{50} = 5.3 \pm 0.4 \mu\text{M}$ ; mean  $\pm$  s.d.;  $n=3$ ). (F) Fluorescence response to a single-pulse stimulation in the presence of amphetamine (10  $\mu\text{M}$ ) or the DRD1 antagonist SKF83566 (1  $\mu\text{M}$ ). (G) Estimate of basal DA concentration in the presence of amphetamine at saturated concentration by interpolation on a dose-response curve, normalized to peak value ( $n$  numbers are shown for each concentration).

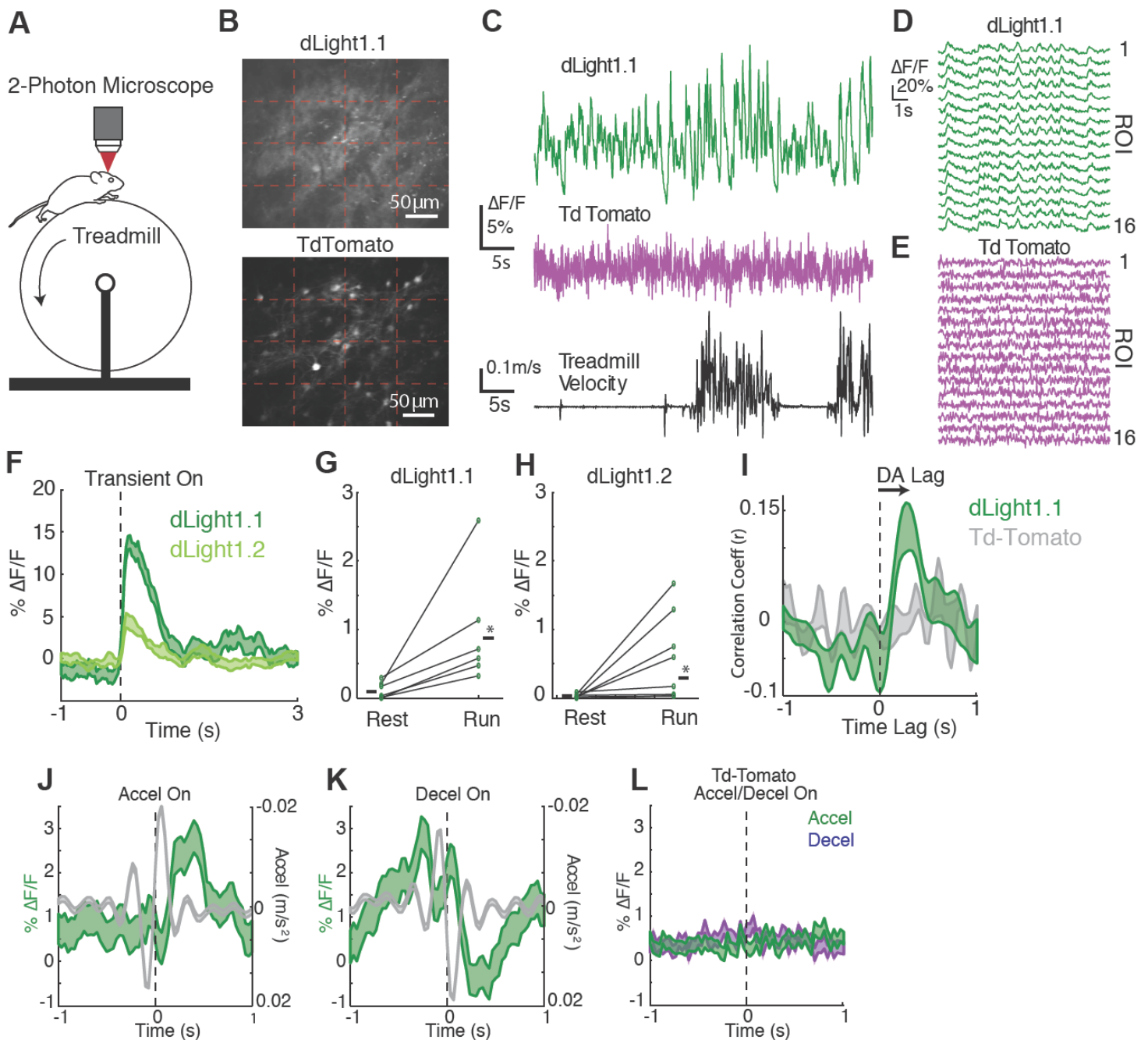


**Fig. S9. Two photon imaging of locomotion related bi-directional dopamine transients in dorsal striatum.** (A) Schematics of two-photon imaging of head-fixed mouse during treadmill locomotion. (B) Mean fluorescence projection from a representative imaging field showing green dLight1.1 expression (top) and red td-Tomato expression (bottom). (C) Average fluorescence changes in the field of whole in green ( $\Delta F/F$ , green, top), red fluorescence (magenta, center), and treadmill velocity (black, bottom) for a representative imaging session. (D-E) Mean  $\Delta F/F$  traces for 16 equal-sized ROIs tiling the imaging field pictured in (C) (red-dashed lines) in green and red. Note large positive-going transients and the high synchrony across ROIs in dLight1.1 fluorescence, but not in td-Tomato fluorescence. (F) Mean  $\Delta F/F$  for all significant positive-going transients in mice expressing either dLight1.1 ( $n = 2$  mice, 131 transients) or dLight1.2 ( $n = 2$  mice, 31 transients). (G-H) Mean transient  $\Delta F/F$  during rest and run for all fields in dLight1.1 ( $n = 2$  mice, 5 fields) and dLight1.2 ( $n = 2$  mice, 8 fields) (I) Cross correlation between acceleration and  $\Delta F/F$  for dLight1.1 during run periods (peak mean cross correlation 240ms). (J-L) DA transients were rapidly and bi-directionally modulated by accelerations and decelerations. Mean  $\Delta F/F$  from dLight1.1 aligned on the zero crossing of all large accelerations (J) or decelerations (K). Note the significant peak in  $\Delta F/F$  following the acceleration peak (J) or the decrease below baseline following decelerations (K). (L) Same as (J, K) but for the td-Tomato traces. Note the lack of significant peaks or troughs to accelerations or decelerations. Shaded regions and error bars indicate SEM. Asterisks indicate  $p < 0.0001$  with Wilcoxon rank-sum test.

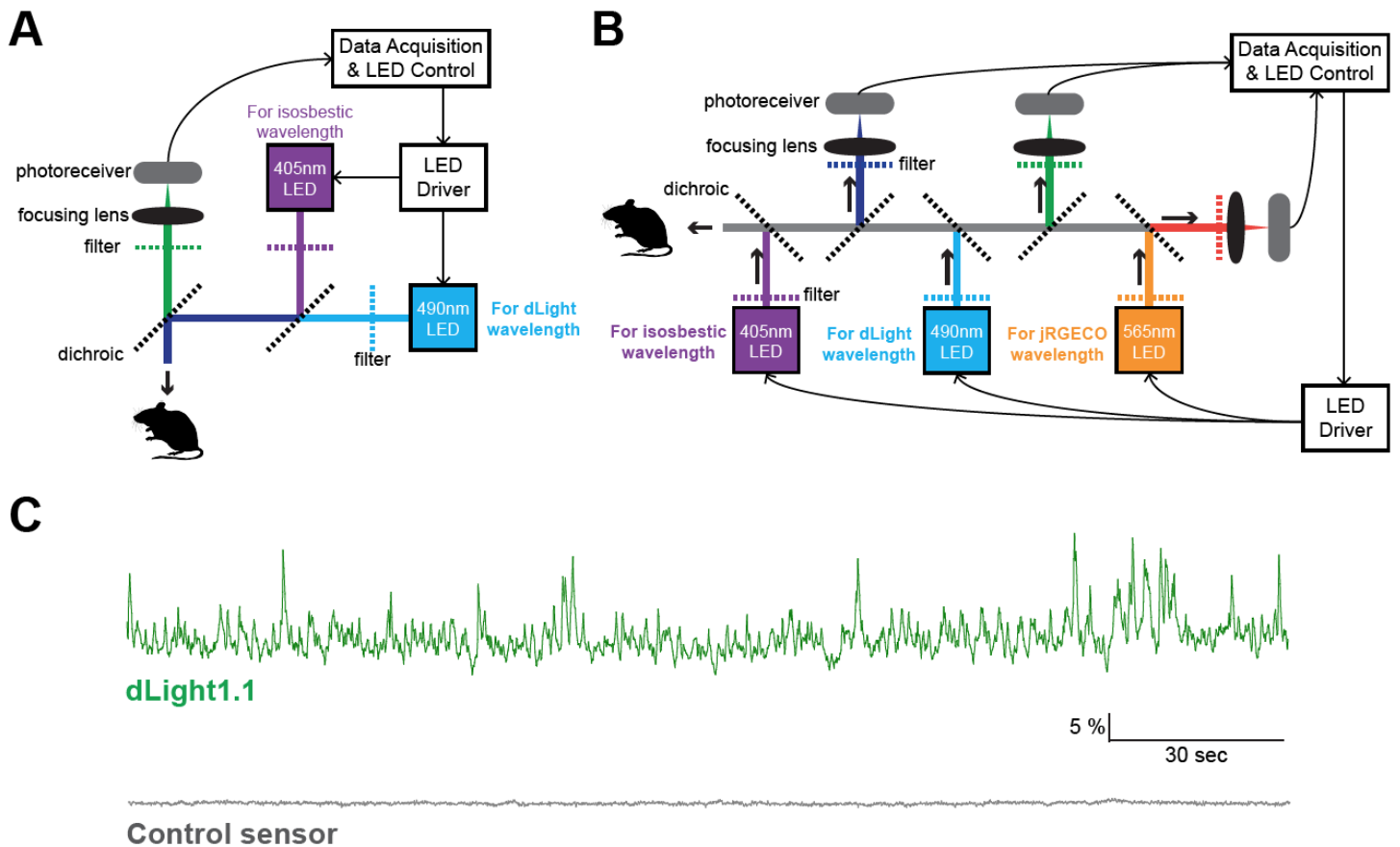


**Fig. S10. Fiber photometry setups and spontaneous DA transients in NAc.** (A) Schematics of fiber photometry setup for dLight1 imaging. Two LEDs were used: 490 nm for dLight1.1 excitation and 405 nm for an isosbestic wavelength (63). These two LEDs were modulated at different frequencies and demodulated with lock-in functions implemented in the custom software. (B) Schematics of “dual color” fiber photometry setup. Compared to conventional fiber photometry, an additional 565 nm LED was added to excite red-shifted  $\text{Ca}^{2+}$  indicator jRGECO1a (31). Emitted fluorescence was divided into three channels based on their spectral profiles, detected by separate photoreceivers and then demodulated. (C) Representative traces of dLight1.1 (green) and control sensor (gray). Note that there are clear fluctuations of fluorescence in dLight1.1 with occasional bursts, while no apparent change of fluorescence is observed with control sensor.

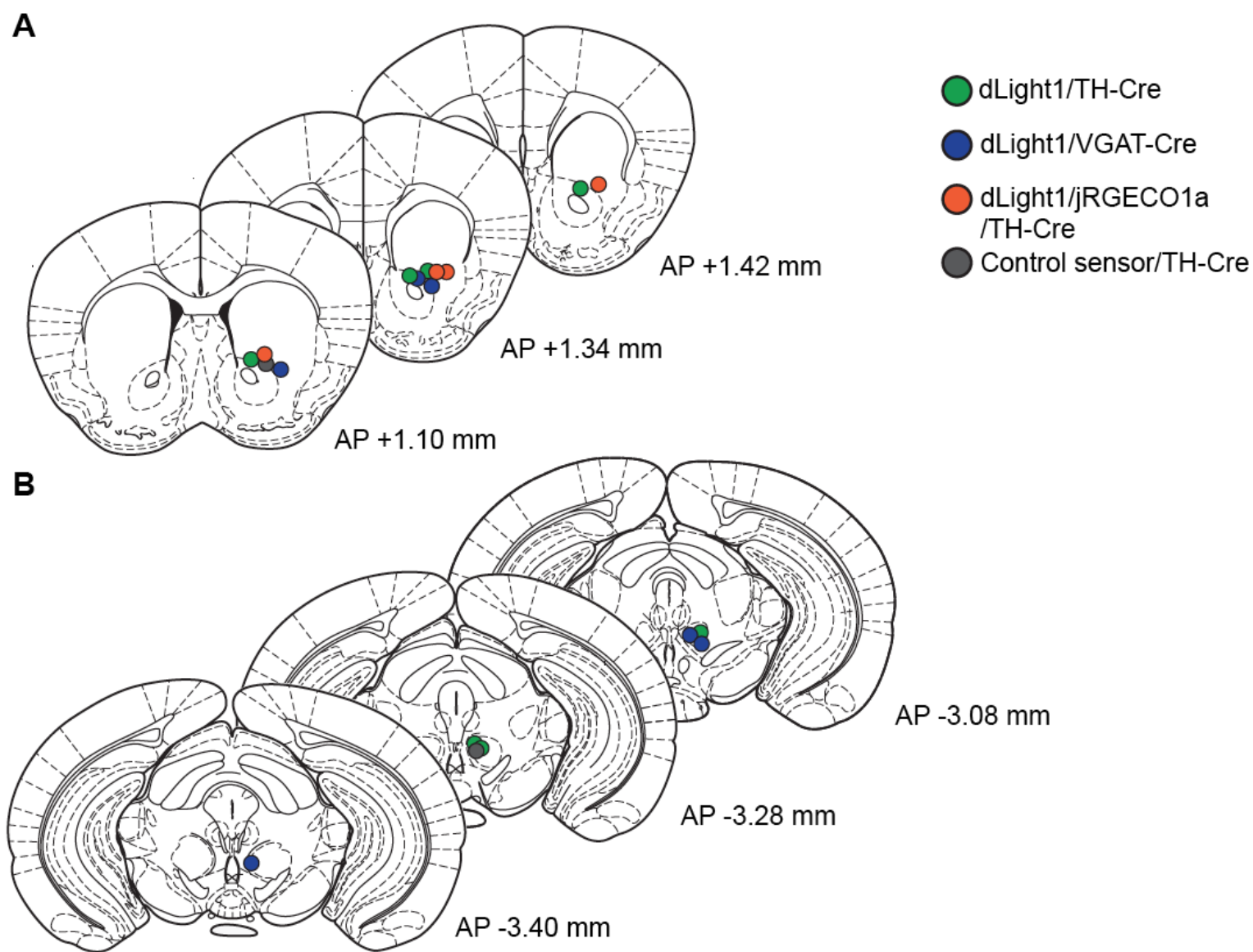


**Fig. S11. Histological verification of fiber tip locations during fiber photometry recordings.** (A) Histologically verified anatomical positions of implanted fibers for photometry in the NAc. (B) Histologically verified anatomical positions of implanted fibers for optogenetic stimulation in the VTA. Histological brain images were reproduced from Paxinos and Franklin's *The Mouse Brain in Stereotaxic Coordinates* (Academic Press, 2012).

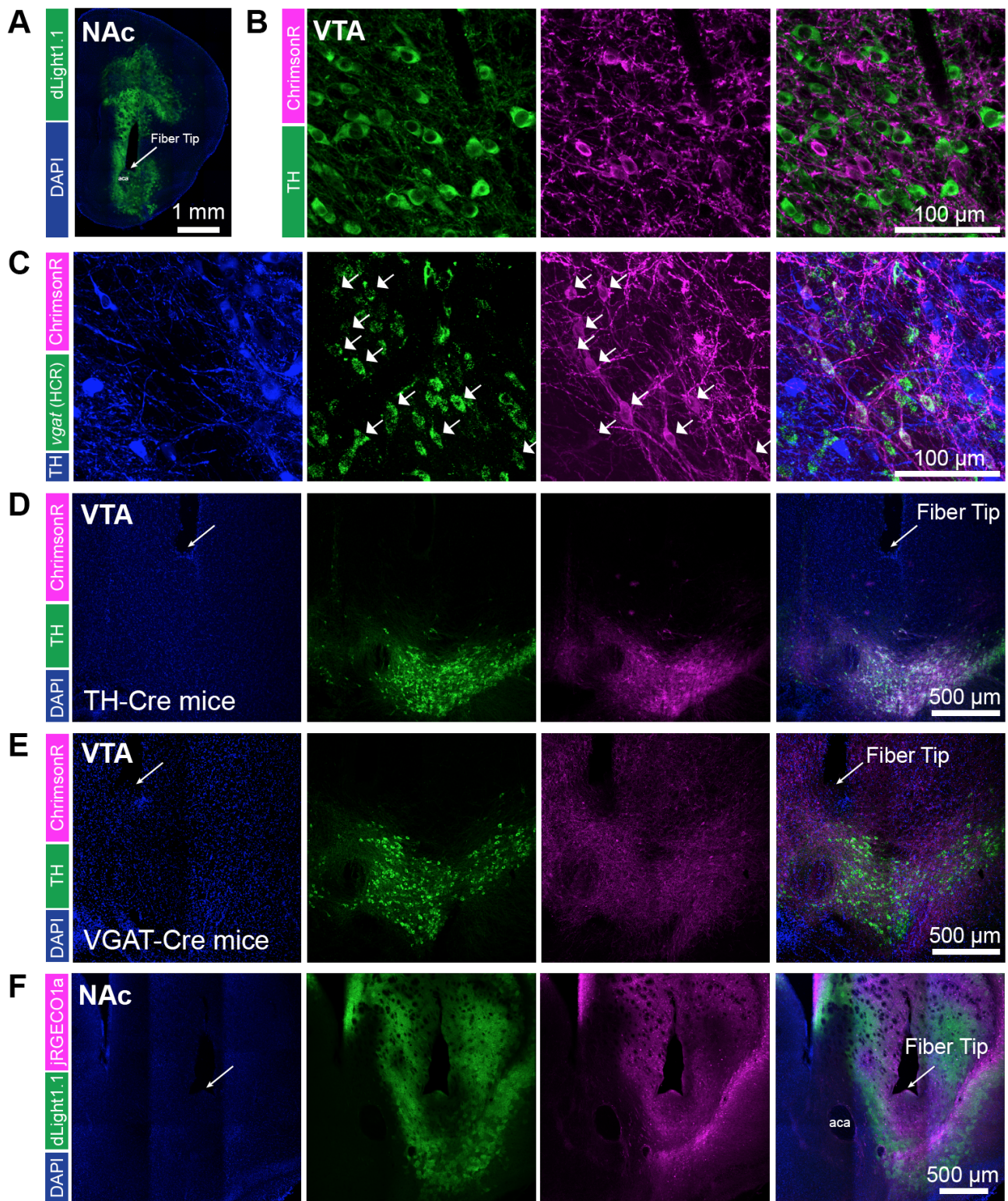


**Fig. S12. Histological verification of virus expression in the NAc and VTA.** (A) Histological image of dLight1.1 (green) expression in the NAc with fiber tip location in a VGAT-Cre mouse. Blue indicates nuclear staining DAPI. (B) Histological images showing that ChromsonR-expressing (magenta) neurons do not overlap with DA (green for tyrosine hydroxylase (TH)<sup>+</sup>) neurons in the VTA. (C) Histological images showing that ChromsonR-expressing (magenta) neurons in the VTA co-localize with *vgat* mRNA (green, detected by hybrid chain reaction in situ hybridization, see supplementary information for details), but not with TH protein (blue, by IHC). Thick arrows indicate neurons co-expressing ChromsonR and *vgat* mRNA. (D) Representative low-magnification images of VTA regions in TH-Cre mice showing optical fiber tip locations (best visible in DAPI section) and virus expressions in the VTA. Blue is DAPI, green TH<sup>+</sup> DA neurons, and magenta ChromsonR<sup>+</sup> neurons. (E) Same as (D) above, but for a VGAT-Cre mice. (F) Histological images of a NAc region with co-expression of dLight1.1 (green) and jRGECO1a (magenta).

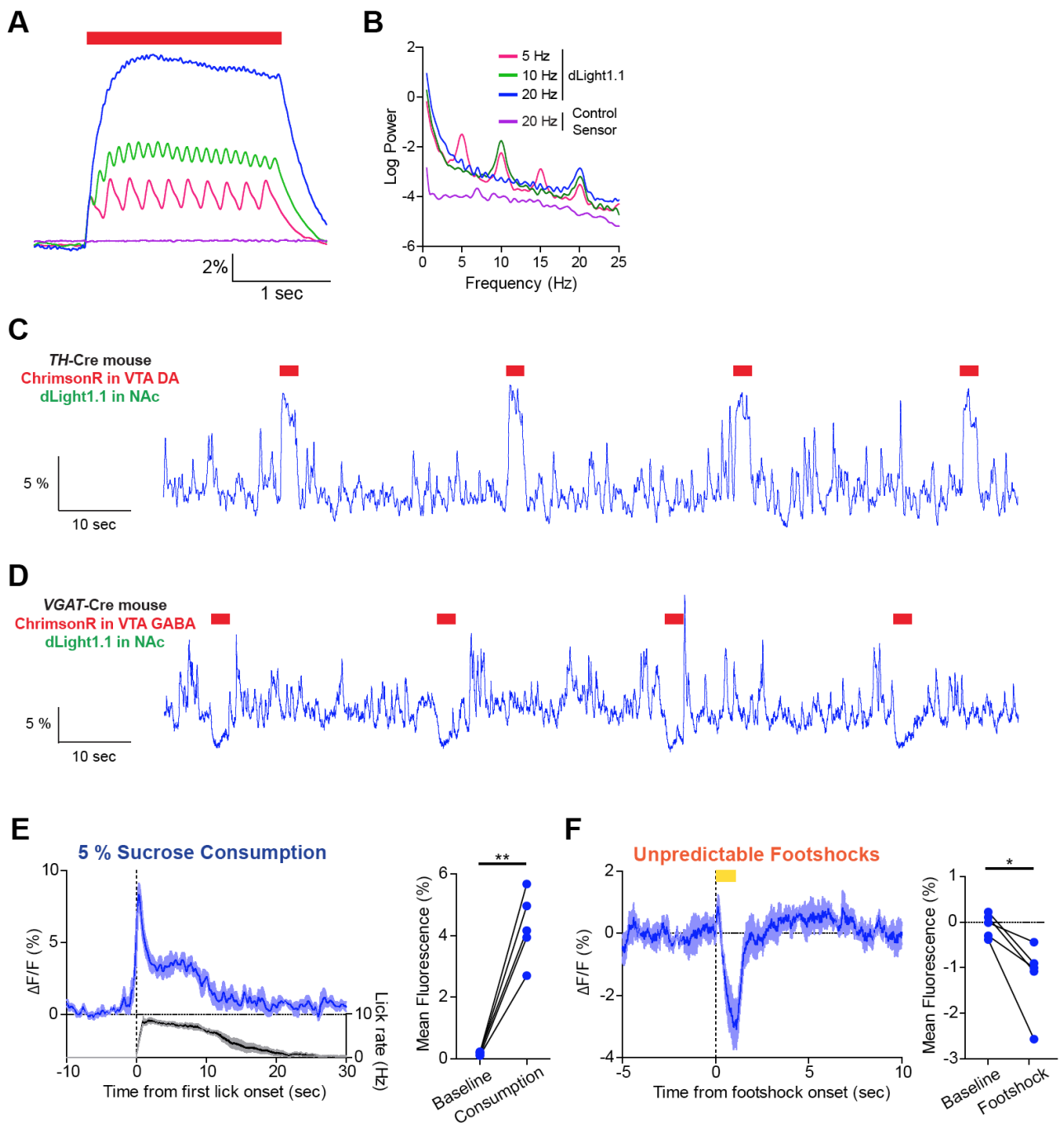


**Fig. S13. dLight1 fluorescence in response to optogenetic stimulation of VTA DA or GABA neurons and NAc DA dynamics underlying natural behaviors.** (A) Magnified version of traces in **Fig. 3D**. Note that there are clear peaks of DA transients corresponding to each optogenetic stimulation pulses, even at 20 Hz. (B) Power spectral density analysis reveals peaks at matching stimulation frequencies (and harmonics) in dLight1.1, while the control sensor shows no clear peak in any frequency ranges. (C) Raw trace of a TH-Cre mouse expressing dLight1.1 during VTA DA photostimulation. Optogenetic stimulation of VTA DA neurons caused evident and time-locked increase in fluorescence from spontaneously fluctuating transients. (D) Raw trace of a VGAT-Cre mouse expressing dLight1.1 during VTA GABA photostimulation. Fluorescence is decreased from baseline fluctuations upon optogenetic stimulation of VTA GABA neurons. (E) DA dynamics during natural behavior recorded from conventional fiber photometry with separate mouse cohort expressing dLight1.1 alone in the NAc. Mice consumed 5% sucrose water. Consistent with dual color fiber photometry results shown in **Fig 3M** and voluntary reward consumption was associated with increase of dLight1.1 fluorescence (mean fluorescence increase was quantified; paired t-test,  $t_4 = 8.495$ ,  $p = 0.0011$ ). (F) DA dynamics while mice expressing dLight1.1 only in the NAc received unpredictable footshocks. Footshock caused transient depression of dLight1.1 fluorescence, which is consistent with dual color fiber photometry results shown in **Fig 3O** (mean fluorescence decrease were quantified; paired t-test,  $t_4 = 3.765$ ,  $p = 0.0197$ ).

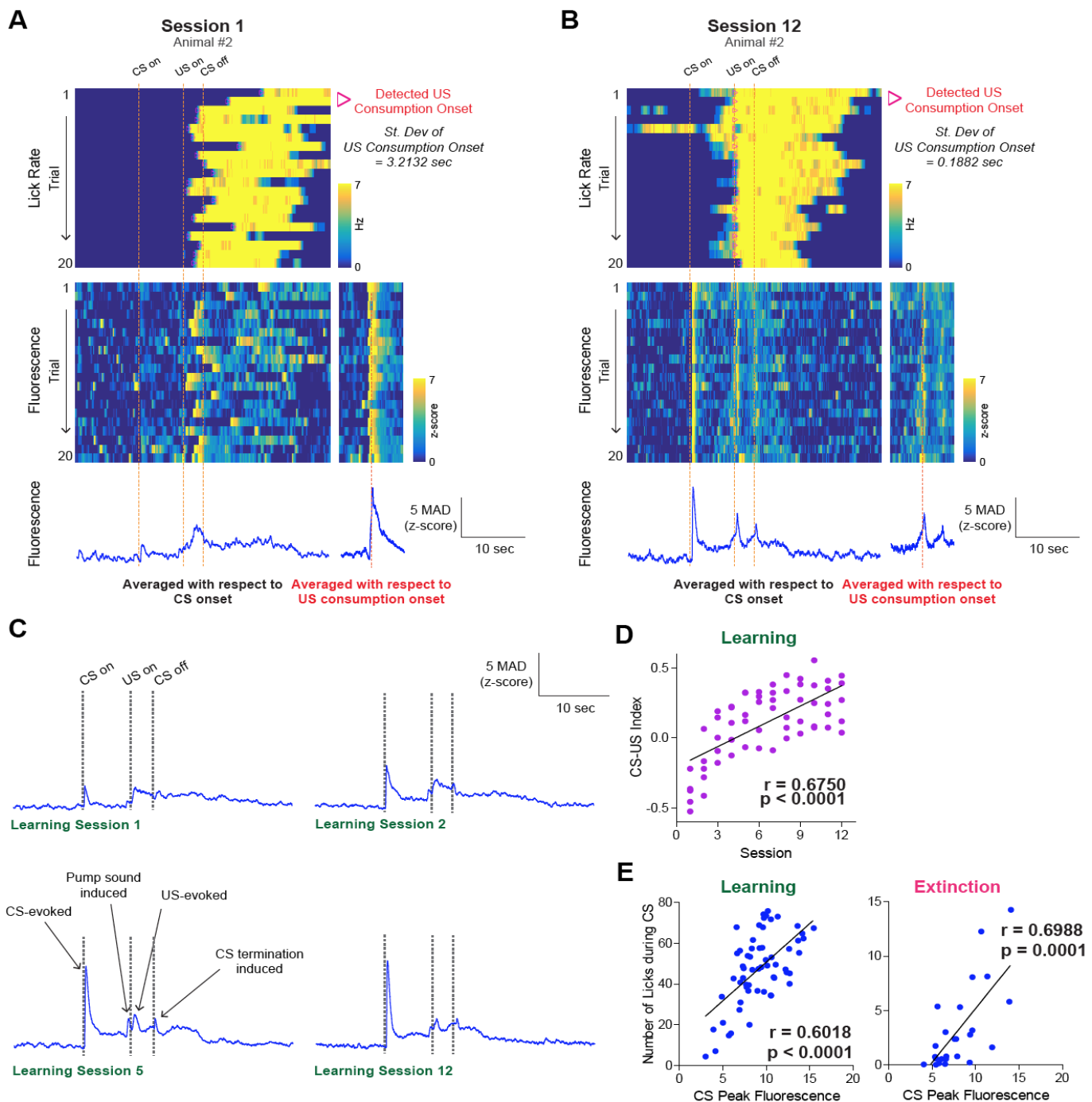


**Fig. S14. Detection of US consumption onsets and details of DA dynamics after learning.** (A) Individual trial heatmap data of lick rate (top) and fluorescence (bottom) from a mouse in learning session 1. Notice that lick onsets (indicated as magenta triangles or sudden color change from blue to yellow) are highly variable in this early session. When fluorescence is averaged from CS onset, fluorescence response from US is averaged or canceled out. However, when fluorescence is averaged from US consumption onset (defined as lick onset after US is available), fluorescence peaks are aligned and results in higher US response. (B) Same as (A), but from learning session 12. After cue-reward association, mice show anticipatory lick behaviors in most of trials, therefore most lick onsets correspond to the time when US is available ( $t = 7$  s after CS onset or second dotted line). Therefore, US response values are almost identical when fluorescence are averaged from CS onset or US consumption onset. (C) Averaged photometry traces from learning sessions 1, 2, 5, and 12. We observed total of four peaks in dLight1 fluorescence (best visible at the session 5): 1) CS-evoked (right after time = 0, which was dynamically modulated across learning and extinction), 2) pump sound induced (after time = 6), 3) US-evoked (after time = 7) and 4) CS termination induced (after time = 10) peaks. (D) CS-US index (see supplementary information for definition) increases across learning sessions, suggesting that fluorescence response is transferred from US to CS. (E) Positive correlations between CS peak fluorescence and licks during CS presentation, both in learning (left) and extinction (right) sessions.

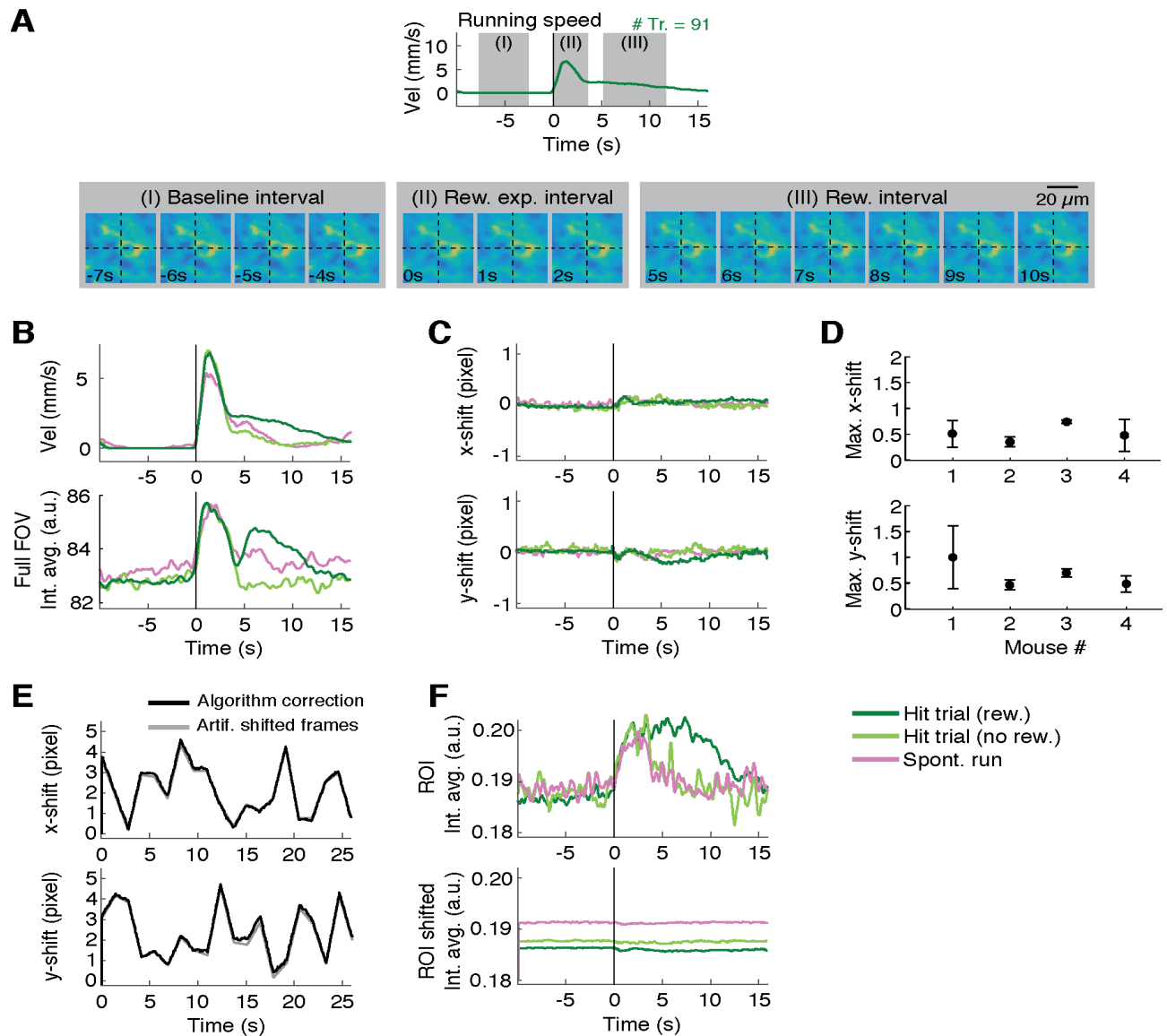


**Fig. S15. Cortical dLight1 transients during animal behavior cannot be explained by image motion artifacts.** (A) Top, average mouse running velocity for rewarded “Hit trials” from an example recording session. Data were aligned to running onset (vertical black line) prior to averaging. Three time intervals are indicated: “(I) Baseline interval” is part of the interval during which the animal was required to stand still; “(II) Reward expectation interval” defines the interval during which the mouse began to run and expected a reward; and “(III) Reward interval” defines the period during which the water reward was delivered in 80% of “Hit trials”. Bottom, 40x45 pixel detail from the corresponding time-lapse fluorescence imaging data. Image data was motion corrected prior to averaging (Methods). Image comparison (dotted crosshair) indicates that residual image movement was below one pixel within and across the baseline, reward expectation, and reward intervals. (B) Top, average mouse running velocity from the same recording session but for all trial types. Bottom, corresponding dLight1.2 fluorescence transients across the entire field of view (FOV). Data was motion corrected prior to averaging. Full FOV transients retain the main characteristics of the single ROI transients (Fig. 5E), but details about the spatio-temporal heterogeneity of DA release are lost. (C) Lateral image displacements detected by the motion correction algorithm for the example average data shown in panel B. Image displacements were below one pixel for all trial types. (D) Maximum lateral image displacements for all averaged recording sessions and all mice. Error bars indicate SEM. (E) The motion correction algorithm reliably detected sub- and supra-pixel image displacements. Artificially introduced shifts (grey) to the data shown in panels A-C were tracked by the algorithm with sub-pixel precision (black). (F) Top, task-related dLight1.2 fluorescence transients plotted as intensity average from an example ROI (from fig. S16G). Bottom, transients extracted from the same ROI when applied to an artificially generated dataset in which the first frame of the top panel dataset was displaced using the lateral residual shifts shown in panel C. Intensity average transients produced by image shifts to the static first frame are negligibly small and distinct from task-related fluorescence transients.

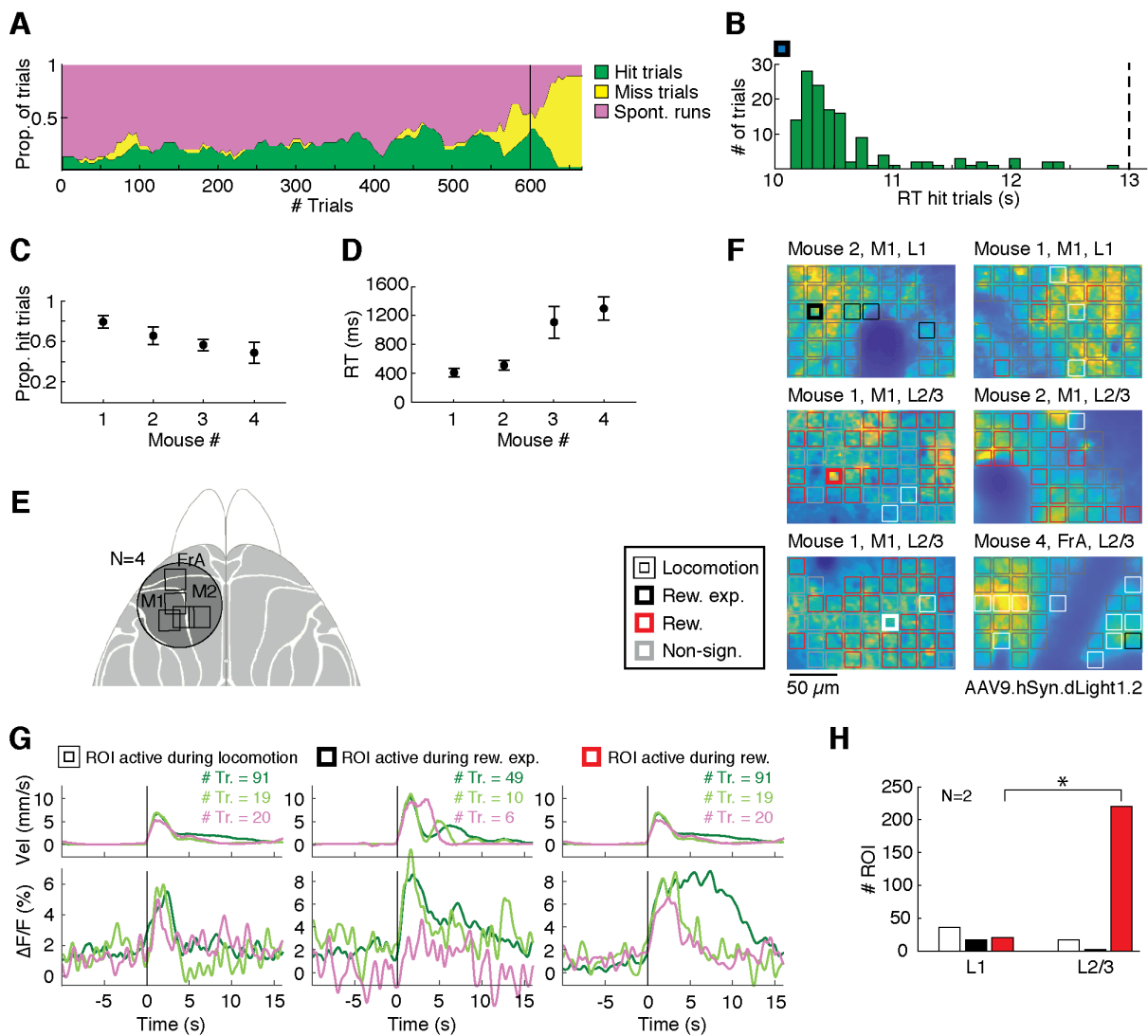


**Fig. S16. Behavioral performance and single-session dLight1 transients during cortical two-photon imaging. (A-D)** Mouse performance on the visuomotor association task during imaging sessions. **(A)** Example performance data from one recording session. Out of all trials in which the “Go” stimulus was presented, the proportion of “Hit trials” (green) was >80%. The “Go” stimulus was not presented in “Spontaneous runs” (pink) during the stand-still phase. Animals typically performed the task successfully for several hundred trials before a step increase in “Miss trials” (yellow) indicated that they had lost interest in the water reward. Trials beyond that point (black vertical line) were excluded from analysis. **(B)** Reaction times (RT) from an example recording session. Most “Go” stimulus-triggered runs happened within the first second after stimulus onset indicating that the mouse had learned the task. The dashed line at 13s indicates the “Go” stimulus offset. **(C)** Population data showing mean proportion of “Hit trials” for all mice (N=4) and recording sessions (mouse #1: 4 sessions; mouse #2: 9 sessions; mouse #3: 2 sessions; mouse #4: 4 sessions). **(D)** Mean RTs for all mice and recording sessions. Error bars in panel C and D indicate SEM. **(E)** Dorsal view of the mouse cortex with the imaging locations (square) from all mice indicated. **(F)** Example fluorescence image details showing dLight1.2 expression pattern for different mice and recording locations: M1 cortex, layer 1 and layer 2/3; FrA cortex, layer 2/3. The computationally defined regions of interest (ROIs), colored based on their response type, are overlaid. Single-session fluorescence transients of the highlighted ROIs (bold outlines) are shown in panel G. **(G)** Representative task-related dLight1.2 fluorescence transients from example recording sessions (population averages are shown in Fig. 5E). Top, mouse running speed on the spherical treadmill. Bottom, three common types of task-related fluorescence transients in M1. Left, example ROI showing significantly increased dLight1.2 fluorescence during locomotion but not reward; middle, ROI significantly active during reward expectation but not locomotion; right, ROI with significantly increased dLight1.2 fluorescence during the reward. Each colored trace is an average of the indicated number of trials aligned to running onset (vertical black line).  $p < 0.05$ , Wilcoxon test, Bonferroni corrected for multiple comparisons. **(H)** Population data showing the number of ROIs with significant dLight1 transients in layer 1 (L1) and layer 2/3 (L2/3) of area M1 sorted by the three response types (see panel G and Fig. 5E). Significantly more reward related responses are seen in deeper layers. \* indicates significance, Binomial test,  $p < 0.05$ , adjusted for total number of ROIs recorded in the respective layer.

**Data S1. (separate file)**

Sequences of the constructs used in this study.

**Data S2. (separate file)**

Data info for Figure 1-2.

**Data S3. (separate file)**

Data info for Figure 5.

## References

1. N. X. Tritsch, B. L. Sabatini, Dopaminergic modulation of synaptic transmission in cortex and striatum. *Neuron* **76**, 33–50 (2012). [doi:10.1016/j.neuron.2012.09.023](https://doi.org/10.1016/j.neuron.2012.09.023) [Medline](#)
2. R. A. Wise, Dopamine, learning and motivation. *Nat. Rev. Neurosci.* **5**, 483–494 (2004). [doi:10.1038/nrn1406](https://doi.org/10.1038/nrn1406) [Medline](#)
3. J. T. Dudman, J. W. Krakauer, The basal ganglia: From motor commands to the control of vigor. *Curr. Opin. Neurobiol.* **37**, 158–166 (2016). [doi:10.1016/j.conb.2016.02.005](https://doi.org/10.1016/j.conb.2016.02.005) [Medline](#)
4. W. Schultz, P. Dayan, P. R. Montague, A neural substrate of prediction and reward. *Science* **275**, 1593–1599 (1997). [doi:10.1126/science.275.5306.1593](https://doi.org/10.1126/science.275.5306.1593) [Medline](#)
5. S. H. Lee, Y. Dan, Neuromodulation of brain states. *Neuron* **76**, 209–222 (2012). [doi:10.1016/j.neuron.2012.09.012](https://doi.org/10.1016/j.neuron.2012.09.012) [Medline](#)
6. E. Marder, Neuromodulation of neuronal circuits: Back to the future. *Neuron* **76**, 1–11 (2012). [doi:10.1016/j.neuron.2012.09.010](https://doi.org/10.1016/j.neuron.2012.09.010) [Medline](#)
7. W. Schultz, Dopamine reward prediction-error signalling: A two-component response. *Nat. Rev. Neurosci.* **17**, 183–195 (2016). [doi:10.1038/nrn.2015.26](https://doi.org/10.1038/nrn.2015.26) [Medline](#)
8. W. X. Pan, R. Schmidt, J. R. Wickens, B. I. Hyland, Dopamine cells respond to predicted events during classical conditioning: Evidence for eligibility traces in the reward-learning network. *J. Neurosci.* **25**, 6235–6242 (2005). [doi:10.1523/JNEUROSCI.1478-05.2005](https://doi.org/10.1523/JNEUROSCI.1478-05.2005) [Medline](#)
9. J. Y. Cohen, S. Haesler, L. Vong, B. B. Lowell, N. Uchida, Neuron-type-specific signals for reward and punishment in the ventral tegmental area. *Nature* **482**, 85–88 (2012). [doi:10.1038/nature10754](https://doi.org/10.1038/nature10754) [Medline](#)
10. M. W. Howe, D. A. Dombeck, Rapid signalling in distinct dopaminergic axons during locomotion and reward. *Nature* **535**, 505–510 (2016). [doi:10.1038/nature18942](https://doi.org/10.1038/nature18942) [Medline](#)
11. G. Cui, S. B. Jun, X. Jin, M. D. Pham, S. S. Vogel, D. M. Lovinger, R. M. Costa, Concurrent activation of striatal direct and indirect pathways during action initiation. *Nature* **494**, 238–242 (2013). [doi:10.1038/nature11846](https://doi.org/10.1038/nature11846) [Medline](#)
12. A. Jaquins-Gerstl, A. C. Michael, A review of the effects of FSCV and microdialysis measurements on dopamine release in the surrounding tissue. *Analyst* **140**, 3696–3708 (2015). [doi:10.1039/C4AN02065K](https://doi.org/10.1039/C4AN02065K) [Medline](#)
13. M. Ganesana, S. T. Lee, Y. Wang, B. J. Venton, Analytical Techniques in Neuroscience: Recent Advances in Imaging, Separation, and Electrochemical Methods. *Anal. Chem.* **89**, 314–341 (2017). [doi:10.1021/acs.analchem.6b04278](https://doi.org/10.1021/acs.analchem.6b04278) [Medline](#)

14. A. Muller, V. Joseph, P. A. Slesinger, D. Kleinfeld, Cell-based reporters reveal in vivo dynamics of dopamine and norepinephrine release in murine cortex. *Nat. Methods* **11**, 1245–1252 (2014). [doi:10.1038/nmeth.3151](https://doi.org/10.1038/nmeth.3151) [Medline](#)
15. D. Lee, M. Creed, K. Jung, T. Stefanelli, D. J. Wendler, W. C. Oh, N. L. Mignocchi, C. Lüscher, H.-B. Kwon, Temporally precise labeling and control of neuromodulatory circuits in the mammalian brain. *Nat. Methods* **14**, 495–503 (2017). [doi:10.1038/nmeth.4234](https://doi.org/10.1038/nmeth.4234) [Medline](#)
16. C. P. Ford, P. E. Phillips, J. T. Williams, The time course of dopamine transmission in the ventral tegmental area. *J. Neurosci.* **29**, 13344–13352 (2009). [doi:10.1523/JNEUROSCI.3546-09.2009](https://doi.org/10.1523/JNEUROSCI.3546-09.2009) [Medline](#)
17. C. P. Ford, S. C. Gantz, P. E. Phillips, J. T. Williams, Control of extracellular dopamine at dendrite and axon terminals. *J. Neurosci.* **30**, 6975–6983 (2010). [doi:10.1523/JNEUROSCI.1020-10.2010](https://doi.org/10.1523/JNEUROSCI.1020-10.2010) [Medline](#)
18. T. W. Chen, T. J. Wardill, Y. Sun, S. R. Pulver, S. L. Renninger, A. Baohan, E. R. Schreiter, R. A. Kerr, M. B. Orger, V. Jayaraman, L. L. Looger, K. Svoboda, D. S. Kim, Ultrasensitive fluorescent proteins for imaging neuronal activity. *Nature* **499**, 295–300 (2013). [doi:10.1038/nature12354](https://doi.org/10.1038/nature12354) [Medline](#)
19. J. S. Marvin, B. G. Borghuis, L. Tian, J. Cichon, M. T. Harnett, J. Akerboom, A. Gordus, S. L. Renninger, T.-W. Chen, C. I. Bargmann, M. B. Orger, E. R. Schreiter, J. B. Demb, W.-B. Gan, S. A. Hires, L. L. Looger, An optimized fluorescent probe for visualizing glutamate neurotransmission. *Nat. Methods* **10**, 162–170 (2013). [doi:10.1038/nmeth.2333](https://doi.org/10.1038/nmeth.2333) [Medline](#)
20. A. Manglik, T. H. Kim, M. Masureel, C. Altenbach, Z. Yang, D. Hilger, M. T. Lerch, T. S. Kobilka, F. S. Thian, W. L. Hubbell, R. S. Prosser, B. K. Kobilka, Structural Insights into the Dynamic Process of  $\beta$ 2-Adrenergic Receptor Signaling. *Cell* **161**, 1101–1111 (2015). [doi:10.1016/j.cell.2015.04.043](https://doi.org/10.1016/j.cell.2015.04.043) [Medline](#)
21. S. G. Rasmussen, B. T. DeVree, Y. Zou, A. C. Kruse, K. Y. Chung, T. S. Kobilka, F. S. Thian, P. S. Chae, E. Pardon, D. Calinski, J. M. Mathiesen, S. T. A. Shah, J. A. Lyons, M. Caffrey, S. H. Gellman, J. Steyaert, G. Skiniotis, W. I. Weis, R. K. Sunahara, B. K. Kobilka, Crystal structure of the  $\beta$ 2 adrenergic receptor-Gs protein complex. *Nature* **477**, 549–555 (2011). [doi:10.1038/nature10361](https://doi.org/10.1038/nature10361) [Medline](#)
22. C. D. Strader, I. S. Sigal, M. R. Candelore, E. Rands, W. S. Hill, R. A. Dixon, Conserved aspartic acid residues 79 and 113 of the beta-adrenergic receptor have different roles in receptor function. *J. Biol. Chem.* **263**, 10267–10271 (1988). [Medline](#)
23. R. Irannejad, J. C. Tomshine, J. R. Tomshine, M. Chevalier, J. P. Mahoney, J. Steyaert, S. G. F. Rasmussen, R. K. Sunahara, H. El-Samad, B. Huang, M. von Zastrow, Conformational

- biosensors reveal GPCR signalling from endosomes. *Nature* **495**, 534–538 (2013).  
[doi:10.1038/nature12000](https://doi.org/10.1038/nature12000) [Medline](#)
24. R. G. Vickery, M. von Zastrow, Distinct dynamin-dependent and -independent mechanisms target structurally homologous dopamine receptors to different endocytic membranes. *J. Cell Biol.* **144**, 31–43 (1999). [doi:10.1083/jcb.144.1.31](https://doi.org/10.1083/jcb.144.1.31) [Medline](#)
25. J. T. Yorgason, D. M. Zeppenfeld, J. T. Williams, Cholinergic Interneurons Underlie Spontaneous Dopamine Release in Nucleus Accumbens. *J. Neurosci.* **37**, 2086–2096 (2017). [doi:10.1523/JNEUROSCI.3064-16.2017](https://doi.org/10.1523/JNEUROSCI.3064-16.2017) [Medline](#)
26. N. A. Courtney, C. P. Ford, The timing of dopamine- and noradrenaline-mediated transmission reflects underlying differences in the extent of spillover and pooling. *J. Neurosci.* **34**, 7645–7656 (2014). [doi:10.1523/JNEUROSCI.0166-14.2014](https://doi.org/10.1523/JNEUROSCI.0166-14.2014) [Medline](#)
27. A. A. Mamaligas, Y. Cai, C. P. Ford, Nicotinic and opioid receptor regulation of striatal dopamine D2-receptor mediated transmission. *Sci. Rep.* **6**, 37834 (2016).  
[doi:10.1038/srep37834](https://doi.org/10.1038/srep37834) [Medline](#)
28. L. A. Gunaydin, L. Grosenick, J. C. Finkelstein, I. V. Kauvar, L. E. Fenno, A. Adhikari, S. Lammel, J. J. Mirzabekov, R. D. Airan, K. A. Zalocusky, K. M. Tye, P. Anikeeva, R. C. Malenka, K. Deisseroth, Natural neural projection dynamics underlying social behavior. *Cell* **157**, 1535–1551 (2014). [doi:10.1016/j.cell.2014.05.017](https://doi.org/10.1016/j.cell.2014.05.017) [Medline](#)
29. K. R. Tan, C. Yvon, M. Turiault, J. J. Mirzabekov, J. Doehner, G. Labouèbe, K. Deisseroth, K. M. Tye, C. Lüscher, GABA neurons of the VTA drive conditioned place aversion. *Neuron* **73**, 1173–1183 (2012). [doi:10.1016/j.neuron.2012.02.015](https://doi.org/10.1016/j.neuron.2012.02.015) [Medline](#)
30. F. Brischoux, S. Chakraborty, D. I. Brierley, M. A. Ungless, Phasic excitation of dopamine neurons in ventral VTA by noxious stimuli. *Proc. Natl. Acad. Sci. U.S.A.* **106**, 4894–4899 (2009). [doi:10.1073/pnas.0811507106](https://doi.org/10.1073/pnas.0811507106) [Medline](#)
31. H. Dana, B. Mohar, Y. Sun, S. Narayan, A. Gordus, J. P. Hasseman, G. Tsegaye, G. T. Holt, A. Hu, D. Walpita, R. Patel, J. J. Macklin, C. I. Bargmann, M. B. Ahrens, E. R. Schreiter, V. Jayaraman, L. L. Looger, K. Svoboda, D. S. Kim, Sensitive red protein calcium indicators for imaging neural activity. *eLife* **5**, e12727 (2016). [doi:10.7554/eLife.12727](https://doi.org/10.7554/eLife.12727) [Medline](#)
32. S. A. Taha, H. L. Fields, Encoding of palatability and appetitive behaviors by distinct neuronal populations in the nucleus accumbens. *J. Neurosci.* **25**, 1193–1202 (2005).  
[doi:10.1523/JNEUROSCI.3975-04.2005](https://doi.org/10.1523/JNEUROSCI.3975-04.2005) [Medline](#)
33. J. J. Day, M. F. Roitman, R. M. Wightman, R. M. Carelli, Associative learning mediates dynamic shifts in dopamine signaling in the nucleus accumbens. *Nat. Neurosci.* **10**, 1020–1028 (2007). [doi:10.1038/mn1923](https://doi.org/10.1038/mn1923) [Medline](#)

34. J. J. Clark, S. G. Sandberg, M. J. Wanat, J. O. Gan, E. A. Horne, A. S. Hart, C. A. Akers, J. G. Parker, I. Willuhn, V. Martinez, S. B. Evans, N. Stella, P. E. M. Phillips, Chronic microensors for longitudinal, subsecond dopamine detection in behaving animals. *Nat. Methods* **7**, 126–129 (2010). [doi:10.1038/nmeth.1412](https://doi.org/10.1038/nmeth.1412) [Medline](#)
35. J. A. da Silva, F. Tecuapetla, V. Paixão, R. M. Costa, Dopamine neuron activity before action initiation gates and invigorates future movements. *Nature* **554**, 244–248 (2018). [doi:10.1038/nature25457](https://doi.org/10.1038/nature25457) [Medline](#)
36. K. D. Piatkevich, E. E. Jung, C. Straub, C. Linghu, D. Park, H.-J. Suk, D. R. Hochbaum, D. Goodwin, E. Pnevmatikakis, N. Pak, T. Kawashima, C.-T. Yang, J. L. Rhoades, O. Shemesh, S. Asano, Y.-G. Yoon, L. Freifeld, J. L. Saulnier, C. Riegler, F. Engert, T. Hughes, M. Drobizhev, B. Szabo, M. B. Ahrens, S. W. Flavell, B. L. Sabatini, E. S. Boyden, A robotic multidimensional directed evolution approach applied to fluorescent voltage reporters. *Nat. Chem. Biol.* **14**, 352–360 (2018). [doi:10.1038/s41589-018-0004-9](https://doi.org/10.1038/s41589-018-0004-9)
37. J. Quan, J. Tian, Circular polymerase extension cloning for high-throughput cloning of complex and combinatorial DNA libraries. *Nat. Protoc.* **6**, 242–251 (2011). [doi:10.1038/nprot.2010.181](https://doi.org/10.1038/nprot.2010.181) [Medline](#)
38. L. Tian, S. A. Hires, T. Mao, D. Huber, M. E. Chiappe, S. H. Chalasani, L. Petreanu, J. Akerboom, S. A. McKinney, E. R. Schreiter, C. I. Bargmann, V. Jayaraman, K. Svoboda, L. L. Looger, Imaging neural activity in worms, flies and mice with improved GCaMP calcium indicators. *Nat. Methods* **6**, 875–881 (2009). [doi:10.1038/nmeth.1398](https://doi.org/10.1038/nmeth.1398) [Medline](#)
39. A. M. Waterhouse, J. B. Procter, D. M. Martin, M. Clamp, G. J. Barton, Jalview Version 2—a multiple sequence alignment editor and analysis workbench. *Bioinformatics* **25**, 1189–1191 (2009). [doi:10.1093/bioinformatics/btp033](https://doi.org/10.1093/bioinformatics/btp033) [Medline](#)
40. Y. Song, F. DiMaio, R. Y.-R. Wang, D. Kim, C. Miles, T. Brunette, J. Thompson, D. Baker, High-resolution comparative modeling with RosettaCM. *Structure* **21**, 1735–1742 (2013). [doi:10.1016/j.str.2013.08.005](https://doi.org/10.1016/j.str.2013.08.005) [Medline](#)
41. V. Cherezov, D. M. Rosenbaum, M. A. Hanson, S. G. F. Rasmussen, F. S. Thian, T. S. Kobilka, H.-J. Choi, P. Kuhn, W. I. Weis, B. K. Kobilka, R. C. Stevens, High-resolution crystal structure of an engineered human beta2-adrenergic G protein-coupled receptor. *Science* **318**, 1258–1265 (2007). [doi:10.1126/science.1150577](https://doi.org/10.1126/science.1150577) [Medline](#)
42. Y. Chen, X. Song, S. Ye, L. Miao, Y. Zhu, R.-G. Zhang, G. Ji, Structural insight into enhanced calcium indicator GCaMP3 and GCaMPJ to promote further improvement. *Protein Cell* **4**, 299–309 (2013). [doi:10.1007/s13238-013-2103-4](https://doi.org/10.1007/s13238-013-2103-4) [Medline](#)
43. B. J. Bender, A. Cisneros 3rd, A. M. Duran, J. A. Finn, D. Fu, A. D. Lokits, B. K. Mueller, A. K. Sangha, M. F. Sauer, A. M. Sevy, G. Sliwoski, J. H. Sheehan, F. DiMaio, J. Meiler, R. Moretti, Protocols for Molecular Modeling with Rosetta3 and RosettaScripts. *Biochemistry* **55**, 4748–4763 (2016). [doi:10.1021/acs.biochem.6b00444](https://doi.org/10.1021/acs.biochem.6b00444) [Medline](#)

44. T. Patriarchi, A. Shen, W. He, M. Baikoghli, R. H. Cheng, Y. K. Xiang, M. A. Coleman, L. Tian, Nanodelivery of a functional membrane receptor to manipulate cellular phenotype. *Sci. Rep.* **8**, 3556 (2018). [doi:10.1038/s41598-018-21863-3](https://doi.org/10.1038/s41598-018-21863-3) [Medline](#)
45. T. Patriarchi, H. Qian, V. Di Biase, Z. A. Malik, D. Chowdhury, J. L. Price, E. A. Hammes, O. R. Buonarati, R. E. Westenbroek, W. A. Catterall, F. Hofmann, Y. K. Xiang, G. G. Murphy, C.-Y. Chen, M. F. Navedo, J. W. Hell, Phosphorylation of Cav1.2 on S1928 uncouples the L-type Ca<sup>2+</sup> channel from the  $\beta$ 2 adrenergic receptor. *EMBO J.* **35**, 1330–1345 (2016). [doi:10.15252/embj.201593409](https://doi.org/10.15252/embj.201593409) [Medline](#)
46. B. G. Robinson, J. R. Bunzow, J. B. Grimm, L. D. Lavis, J. T. Dudman, J. Brown, K. A. Neve, J. T. Williams, Desensitized D2 autoreceptors are resistant to trafficking. *Sci. Rep.* **7**, 4379 (2017). [doi:10.1038/s41598-017-04728-z](https://doi.org/10.1038/s41598-017-04728-z) [Medline](#)
47. L. Stoppini, P. A. Buchs, D. Muller, A simple method for organotypic cultures of nervous tissue. *J. Neurosci. Methods* **37**, 173–182 (1991). [doi:10.1016/0165-0270\(91\)90128-M](https://doi.org/10.1016/0165-0270(91)90128-M) [Medline](#)
48. H. Zhong, G.-M. Sia, T. R. Sato, N. W. Gray, T. Mao, Z. Khuchua, R. L. Huganir, K. Svoboda, Subcellular dynamics of type II PKA in neurons. *Neuron* **62**, 363–374 (2009). [doi:10.1016/j.neuron.2009.03.013](https://doi.org/10.1016/j.neuron.2009.03.013) [Medline](#)
49. N. Otmakhov, J. Lisman, Measuring CaMKII concentration in dendritic spines. *J. Neurosci. Methods* **203**, 106–114 (2012). [doi:10.1016/j.jneumeth.2011.09.022](https://doi.org/10.1016/j.jneumeth.2011.09.022) [Medline](#)
50. L. Vong, C. Ye, Z. Yang, B. Choi, S. Chua Jr., B. B. Lowell, Leptin action on GABAergic neurons prevents obesity and reduces inhibitory tone to POMC neurons. *Neuron* **71**, 142–154 (2011). [doi:10.1016/j.neuron.2011.05.028](https://doi.org/10.1016/j.neuron.2011.05.028) [Medline](#)
51. J. Lindeberg, D. Usoskin, H. Bengtsson, A. Gustafsson, A. Kylberg, S. Söderström, T. Ebendal, Transgenic expression of Cre recombinase from the tyrosine hydroxylase locus. *Genesis* **40**, 67–73 (2004). [doi:10.1002/gene.20065](https://doi.org/10.1002/gene.20065) [Medline](#)
52. Y. Tufail, D. Cook, L. Furgeaud, C. J. Powers, K. Merten, C. L. Clark, E. Hoffman, A. Ngo, K. J. Sekiguchi, C. C. O’Shea, G. Lemke, A. Nimmerjahn, Phosphatidylserine Exposure Controls Viral Innate Immune Responses by Microglia. *Neuron* **93**, 574–586.e8 (2017). [doi:10.1016/j.neuron.2016.12.021](https://doi.org/10.1016/j.neuron.2016.12.021)
53. A. Matsui, B. C. Jarvie, B. G. Robinson, S. T. Hentges, J. T. Williams, Separate GABA afferents to dopamine neurons mediate acute action of opioids, development of tolerance, and expression of withdrawal. *Neuron* **82**, 1346–1356 (2014). [doi:10.1016/j.neuron.2014.04.030](https://doi.org/10.1016/j.neuron.2014.04.030) [Medline](#)
54. J. A. Cardin, M. Carlén, K. Meletis, U. Knoblich, F. Zhang, K. Deisseroth, L.-H. Tsai, C. I. Moore, Targeted optogenetic stimulation and recording of neurons in vivo using cell-type-specific expression of Channelrhodopsin-2. *Nat. Protoc.* **5**, 247–254 (2010). [doi:10.1038/nprot.2009.228](https://doi.org/10.1038/nprot.2009.228) [Medline](#)

55. G. J. Goldey, D. K. Roumis, L. L. Glickfeld, A. M. Kerlin, R. C. Reid, V. Bonin, D. P. Schafer, M. L. Andermann, Removable cranial windows for long-term imaging in awake mice. *Nat. Protoc.* **9**, 2515–2538 (2014). [doi:10.1038/nprot.2014.165](https://doi.org/10.1038/nprot.2014.165) [Medline](#)
56. W. F. Asaad, E. N. Eskandar, A flexible software tool for temporally-precise behavioral control in Matlab. *J. Neurosci. Methods* **174**, 245–258 (2008). [doi:10.1016/j.jneumeth.2008.07.014](https://doi.org/10.1016/j.jneumeth.2008.07.014) [Medline](#)
57. W. F. Asaad, N. Santhanam, S. McClellan, D. J. Freedman, High-performance execution of psychophysical tasks with complex visual stimuli in MATLAB. *J. Neurophysiol.* **109**, 249–260 (2013). [doi:10.1152/jn.00527.2012](https://doi.org/10.1152/jn.00527.2012) [Medline](#)
58. N. Eshel, M. Bukwich, V. Rao, V. Hemmelder, J. Tian, N. Uchida, Arithmetic and local circuitry underlying dopamine prediction errors. *Nature* **525**, 243–246 (2015). [doi:10.1038/nature14855](https://doi.org/10.1038/nature14855) [Medline](#)
59. J. Park, P. Takmakov, R. M. Wightman, In vivo comparison of norepinephrine and dopamine release in rat brain by simultaneous measurements with fast-scan cyclic voltammetry. *J. Neurochem.* **119**, 932–944 (2011). [doi:10.1111/j.1471-4159.2011.07494.x](https://doi.org/10.1111/j.1471-4159.2011.07494.x) [Medline](#)
60. T. A. Pologruto, B. L. Sabatini, K. Svoboda, ScanImage: Flexible software for operating laser scanning microscopes. *Biomed. Eng. Online* **2**, 13 (2003). [doi:10.1186/1475-925X-2-13](https://doi.org/10.1186/1475-925X-2-13) [Medline](#)
61. M. E. J. Sheffield, M. D. Adoff, D. A. Dombeck, Increased Prevalence of Calcium Transients across the Dendritic Arbor during Place Field Formation. *Neuron* **96**, 490–504.e5 (2017). [doi:10.1016/j.neuron.2017.09.029](https://doi.org/10.1016/j.neuron.2017.09.029)
62. D. A. Dombeck, C. D. Harvey, L. Tian, L. L. Looger, D. W. Tank, Functional imaging of hippocampal place cells at cellular resolution during virtual navigation. *Nat. Neurosci.* **13**, 1433–1440 (2010). [doi:10.1038/nn.2648](https://doi.org/10.1038/nn.2648) [Medline](#)
63. T. N. Lerner, C. Shilyansky, T. J. Davidson, K. E. Evans, K. T. Beier, K. A. Zalocusky, A. K. Crow, R. C. Malenka, L. Luo, R. Tomer, K. Deisseroth, Intact-Brain Analyses Reveal Distinct Information Carried by SNc Dopamine Subcircuits. *Cell* **162**, 635–647 (2015). [doi:10.1016/j.cell.2015.07.014](https://doi.org/10.1016/j.cell.2015.07.014) [Medline](#)
64. J. R. Cho, J. B. Treweek, J. E. Robinson, C. Xiao, L. R. Bremner, A. Greenbaum, V. Gradinaru, Dorsal Raphe Dopamine Neurons Modulate Arousal and Promote Wakefulness by Salient Stimuli. *Neuron* **94**, 1205–1219.e8 (2017). [doi:10.1016/j.neuron.2017.05.020](https://doi.org/10.1016/j.neuron.2017.05.020)
65. H. M. Choi, V. A. Beck, N. A. Pierce, Next-generation in situ hybridization chain reaction: Higher gain, lower cost, greater durability. *ACS Nano* **8**, 4284–4294 (2014). [doi:10.1021/nn405717p](https://doi.org/10.1021/nn405717p) [Medline](#)

66. H. M. T. Choi, M. Schwarzkopf, M. E. Fornace, A. Acharya, G. Artavanis, J. Stegmaier, A. Cunha, N. A. Pierce, Third-generation in situ hybridization chain reaction: Multiplexed, quantitative, sensitive, versatile, robust. *bioRxiv* 285213 [preprint]. 19 March 2018. <https://doi.org/10.1101/285213>
67. S. Shah, E. Lubeck, M. Schwarzkopf, T.-F. He, A. Greenbaum, C. H. Sohn, A. Lignell, H. M. T. Choi, V. Gradinaru, N. A. Pierce, L. Cai, Single-molecule RNA detection at depth by hybridization chain reaction and tissue hydrogel embedding and clearing. *Development* **143**, 2862–2867 (2016). [doi:10.1242/dev.138560](https://doi.org/10.1242/dev.138560) [Medline](#)